

Topological insulators in longitudinally driven waveguides: Lieb and Kagome lattices

Mark J. Ablowitz and Justin T. Cole¹

¹*Department of Applied Mathematics, University of Colorado, Boulder, Colorado 80309*
(Dated: March 12, 2019)

Topological insulators are studied via tight-binding approximations of longitudinally driven photonic lattices with three lattice sites per unit cell. Two cases are considered in detail: Lieb and Kagome lattices. The lattice is decomposed into three sublattices each of which are allowed move independently of one another. Emphasis is placed on periodic driving induced by laser-etched helical coils along the direction of propagation. The linear Floquet bands are constructed for various inter-sublattice rotation patterns such as: different radii, different frequency, phase offset and quasi one-dimensional motion. Depending on the nature of the band structure, bulk spectral bands with nonzero Chern number are found to support topologically protected edge states which can move unidirectionally. In this case, the modes move scatter-free around defects due to underlying topological protection. Intriguing mode dynamics are found including bi-directional topological modes and bulk-edge leakage i.e. excitation of bulk modes at a defect for edge modes with dispersion frequencies nearby the bulk bands. Finally, certain nonlinear edge modes are also found to propagate unidirectionally and scatter-free around lattice defects.

PACS numbers: 42.65.Tg, 42.65.Jx, 42.82.Et

I. INTRODUCTION

The study of photonic topological insulators has received considerable interest due in part to their remarkable mode propagation properties and special connection to underlying topology. In photonic systems, breaking time-reversal symmetry has been shown to support topologically protected states [1]. The bulk bands associated with these systems possess nonzero Chern invariants and, as a result, exhibit so-called gapless bands. Physically, the corresponding modes manifest themselves in edge states that can travel in one direction and propagate stably and without scatter at boundary defects.

The first experimental realization of a topologically protected electromagnetic wave was observed in [2]. In that work an external magnetic field was applied to a periodic array of ferrite rods in order to break time-reversal symmetry. There it was shown that microwaves could be localized along the device boundary, move unidirectionally, and propagate scatter-free around barrier defects.

In the photonic regime, a magnet-free experimental realization of a topological insulator was presented in [3]. In that work time-reversal symmetry was broken by a honeycomb array of helically-varying waveguides etched into a bulk medium. In spatial optics the direction of propagation plays the role of time and so the helical variations act as a time-dependent potential. This paper also focuses on a system of helically-varying waveguides, however here we consider more complicated geometries.

Longitudinally varying waveguide arrays have been used to explore numerous other topological effects. Linear and nonlinear staggered square arrangements were considered in [4] and [5]. By introducing a phase offset among the sublattice waveguides it is possible to observe a topological transition point known as a conical Weyl point [6]. For intense nonlinear beams the edge mode envelope has been found to be governed by a nonlinear

Schrödinger equation and, in certain parameter regimes, support topologically protected edge solitons [7] as well as exhibit modulational instability [8]. Unidirectional edge modes have also been observed to propagate in helically-driven quasicrystals [9]; i.e. structures that are not periodic but contain some long range order.

Applications for these type of systems have been explored. Photonic topological systems have the potential to act as optical isolators (one-way transmitters) [10, 11] and circulators [12]. Different types of photonic topological insulator systems have also been found to generate and support novel and robust laser systems [13–17]. Properties and evolution of high power nonlinear states were investigated in [7] and [18].

In [7] a systematic approach to derive tight-binding models in honeycomb and staggered square lattices (two lattice sites per unit cell) was developed. This paper extends those methods to more complex (three lattice sites per unit cell) periodically driven arrays. In particular, we focus on the Lieb and Kagome lattices. These are two of the simplest 2d lattices possible and they have come up in the context of many important physical systems. Lieb lattices have been used in optical settings (see below) as well as in the study topological spin states of cold fermionic systems [19]. The Kagome lattice has been used as a tunable optical lattice for ultracold atoms [20], and also occurs in materials that are candidates for observing quantum spin liquids [21].

In the absence of external driving both the Lieb and Kagome lattices can support localized flat band modes in the bulk [22–25], or along the edge [22, 26]. Interestingly, flat band modes can be diffraction-free [27]. Introducing uniform helical variation to a Lieb waveguide array has been shown to offer a rich set of edge mode dynamics [26]. These include the presence of a (stationary) flat band mode, as well as (traveling) topologically protected modes. Here we generalize the latter work to allow more

complex sublattice rotation patterns. To our knowledge, edge mode dynamics for helically driven Kagome lattices have been studied much less than the Lieb lattice. We find driven Kagome lattices lead to novel phenomena such as having traveling topological modes which are not always unidirectional.

In this work we decompose the Lieb and Kagome lattices into three sublattices that can move independently of one another and frequently find gapless modes. We derive a tight-binding system, valid in a deep lattice limit, that describes incoming light beams. This model takes into account the lattice driving via periodic functions that are parametrized in terms of the direction of propagation, i.e. the “time” variable. As a result, we obtain a system of differential equations with periodic coefficients of which we compute the Floquet bands, their corresponding eigenmodes/edge modes, and associated topological invariants (Chern numbers). We also briefly consider nonlinear edge modes that exhibit properties of topological protection.

A. Paraxial Wave Equation

The propagation of intense, paraxial light beams in Kerr waveguide arrays is governed by the nonlinear Schrödinger (NLS) equation

$$i \frac{\partial \psi}{\partial z} + \frac{1}{2k_0} \nabla^2 \psi - \frac{k_0}{n_0} (n_\ell(\mathbf{r}, z) - n_2 |\psi|^2) \psi = 0, \quad (1)$$

where k_0 is the carrier wavenumber, n_0 is the bulk media index of refraction, and $\nabla^2 \equiv \partial_x^2 + \partial_y^2$. The complex electric field envelope $\psi(\mathbf{r}, z)$ depends on the position in both the direction of propagation, z , and the transverse plane, $\mathbf{r} = (x, y)$. Regions of high refractive index are carved into bulk media using a femtosecond laser etching process [28]. The presence of these lattice waveguides is represented by the potential function $-n_\ell(\mathbf{r}, z)$. Additionally, focusing Kerr nonlinear media ($n_2 > 0$) exhibits an intensity-dependent response to the incoming light beam. It is directly from equation (1) that we derive our tight-binding system.

In this paper we restrict our attention to non-simple lattices with three lattice sites (a, b, c) per unit cell. To model such a scenario, we rewrite the lattice potential as the combination of three interpenetrating sublattices

$$n_\ell(\mathbf{r}, z) = |\Delta n| \left[1 - V_a(\mathbf{r}, z) - V_b(\mathbf{r}, z) - V_c(\mathbf{r}, z) \right], \quad (2)$$

where $|\Delta n|$ denotes the contrast in waveguide refractive index from that of the bulk. Each sublattice is taken to consist of a sum of Gaussians

$$V_j(\mathbf{r}, z) = \sum_{\mathbf{v} \in \mathcal{R}_j} \tilde{V}(\mathbf{r} - \mathbf{v} - \mathbf{h}_j(z)), \quad j = a, b, c \quad (3)$$

$$\tilde{V}(\mathbf{r}) = \exp\left(-\frac{x^2}{\sigma_x^2} - \frac{y^2}{\sigma_y^2}\right),$$

where $\sigma_x, \sigma_y > 0$. The set \mathcal{R}_j consists of all the lattice sites for the j^{th} sublattice.

The minima of the lattice potential correspond to the center of the waveguides where the index of refraction is largest. The smooth parametric functions $\mathbf{h}_j(z)$ drive the sublattices. The parameters σ_x, σ_y control the geometric shape of the waveguides. When $\sigma_x = \sigma_y$ the waveguides are circular (isotropic), whereas the waveguides are elliptical (anisotropic) when $\sigma_x \neq \sigma_y$.

Here we concentrate on driving functions which are periodic in z . Specifically, we examine

$$\mathbf{h}_j(z) = \tilde{R}_j (\cos(\Lambda_j z + \chi_j), \sin(\Lambda_j z + \chi_j)), \quad (4)$$

where \tilde{R}_j is the helix radius, Λ_j is the angular frequency, and χ_j is an arbitrary phase shift. It is useful to transform to a coordinate frame co-moving with the $V_b(\mathbf{r}, z)$ sublattice by performing the change of variable

$$\tilde{\mathbf{r}} = \mathbf{r} - \mathbf{h}_b(z), \quad \tilde{z} = z.$$

Introducing the transformation

$$\psi(\mathbf{r}, z) = \tilde{\psi}(\tilde{\mathbf{r}}, \tilde{z}) \exp\left(\frac{i \int_0^{\tilde{z}} |\mathbf{A}(\zeta)|^2 d\zeta}{2k_0}\right),$$

for the pseudo-field (vector potential)

$$\mathbf{A}(\tilde{z}) = -k_0 \mathbf{h}'_b(\tilde{z}),$$

yields (after dropping the tilde notation)

$$i \frac{\partial \psi}{\partial z} + \frac{1}{2k_0} (\nabla + i\mathbf{A}(z))^2 \psi - \frac{k_0}{n_0} (n_\ell(\mathbf{r}, z) - n_2 |\psi|^2) \psi = 0. \quad (5)$$

This equation is nondimensionalized by

$$x = \ell x', \quad y = \ell y', \quad z = z_* z',$$

$$\sigma_x = \ell \sigma'_x, \quad \sigma_y = \ell \sigma'_y, \quad \psi = \sqrt{I_*} \psi',$$

where ℓ is the distance between nearest neighbor lattice sites, $z_* = 2k_0 \ell^2$ is a typical propagation distance, and I_* is the peak intensity of the input beam. Dropping the prime notation gives the dimensionless equation

$$i \frac{\partial \psi}{\partial z} + (\nabla + i\mathbf{A}(z))^2 \psi - V(\mathbf{r}, z) \psi + \gamma |\psi|^2 \psi = 0, \quad (6)$$

where $\gamma = 2k_0^2 \ell^2 n_2 I_* / n_0 \geq 0$, with potential function

$$V(\mathbf{r}, z) = V_0^2 \left[1 - V_a(\mathbf{r} - \Delta \mathbf{h}_{ab}(z)) - V_b(\mathbf{r}) - V_c(\mathbf{r} - \Delta \mathbf{h}_{cb}(z)) \right],$$

which has amplitude $V_0^2 = 2k_0^2 \ell^2 |\Delta n| / n_0$, and

$$\Delta \mathbf{h}_{ij}(z) \equiv \mathbf{h}_i(z) - \mathbf{h}_j(z) \quad i, j = a, b, c. \quad (7)$$

In dimensionless form, the driving functions are

$$\mathbf{h}_j(z) = \eta_j (\cos(\Omega_j z + \chi_j), \sin(\Omega_j z + \chi_j)), \quad j = a, b, c$$

where $\eta_j = \tilde{R}_j / \ell$ and $\Omega_j = \Lambda_j z_*$.

Finally, we introduce the phase transformation

$$\psi(\mathbf{r}, z) = \phi(\mathbf{r}, z)e^{-i\mathbf{r}\cdot\mathbf{A}(z)},$$

which simplifies Eq. (6) to

$$i\frac{\partial\phi}{\partial z} + \nabla^2\phi + \mathbf{r}\cdot\mathbf{A}_z\phi - V(\mathbf{r}, z)\phi + \gamma|\phi|^2\phi = 0. \quad (8)$$

The pseudo-field in dimensionless coordinates is given by

$$\mathbf{A}(z) = \kappa(\sin(\Omega_b z + \chi_b), -\cos(\Omega_b z + \chi_b)), \quad (9)$$

(since we are working in the $\mathbf{h}_b(z)$ reference frame) where $\kappa = k_0\ell\tilde{R}_b\Lambda_b$.

II. TIGHT-BINDING APPROXIMATION

We now develop a tight-binding approximation from Eq. (8). This discrete model assumes a sharp contrast of index of refraction between the waveguides and bulk background. Put another way, we are working in a deep lattice regime; i.e. $V_0^2 \gg 1$. In addition, locally we approximate the lattice potential by a paraboloid potential in order to obtain an orbital approximation. The beam field $\phi(\mathbf{r}, z)$ is expressed as a sum of these strongly decaying orbital functions centered at the (z -dependent) lattice sites. The localized orbital modes are taken to satisfy a harmonic oscillator equation with a quadratic potential that is periodic in z . In the deep lattice limit these orbital modes are well-localized so that the only significant interactions occur between nearest neighbors.

Near the well-separated potential minima we approximate the sublattices given in (3) by the first few terms of their Taylor series. The local approximation of the potential is the paraboloid

$$\bar{V}(\mathbf{r}) = V_0^2\left(\frac{x^2}{\sigma_x^2} + \frac{y^2}{\sigma_y^2}\right). \quad (10)$$

Near here the wave field is taken to satisfy the orbital equation

$$[-\nabla^2 + \bar{V}(\mathbf{r} - \mathbf{v}^j - \Delta\mathbf{h}_{jb}(z))] \phi_{j,\mathbf{v}} = E\phi_{j,\mathbf{v}}, \quad j = a, b, c \quad (11)$$

for eigenvalue $E = V_0(1/\sigma_x + 1/\sigma_y)$ and the normalized Gaussian eigenfunction

$$\phi_{j,\mathbf{v}}(\mathbf{r}, z) = \sqrt{\frac{V_0}{\pi\sqrt{\sigma_x\sigma_y}}} \times \exp\left[-\frac{V_0[\mathbf{r} - \mathbf{v}^j - \Delta\mathbf{h}_{jb}(z)]_x^2}{2\sigma_x} - \frac{V_0[\mathbf{r} - \mathbf{v}^j - \Delta\mathbf{h}_{jb}(z)]_y^2}{2\sigma_y}\right], \quad (12)$$

where the subscripts x and y denote the first and second components, respectively and \mathbf{v} denotes the lattice location. The eigenvalue E is the same for each sublattice as long as V_0, σ_x and σ_y are identical in all sublattices.

The wave field is decomposed into a sum of the above orbital functions, given by

$$\phi(\mathbf{r}, z) = \sum_{m,n} [a_{mn}(z)\phi_{a,\mathbf{v}_{mn}}(\mathbf{r}, z) + b_{mn}(z)\phi_{b,\mathbf{v}_{mn}}(\mathbf{r}) + c_{mn}(z)\phi_{c,\mathbf{v}_{mn}}(\mathbf{r}, z)] e^{-iEz}, \quad (13)$$

where the orbitals are modulated by the associated coefficients a_{mn}, b_{mn}, c_{mn} . We substitute expansion (13) into (8), multiply by $\phi_{i,\mathbf{p}}(\mathbf{r}, z)$, $i = a, b, c$, and integrate over all \mathbf{r} . We label the lattice the manner shown in Figs. 1 or 2. The details of a similar derivation are described in [7].

The ansatz in (13) is similar to that used in Wannier functions [29]. Wannier modes are the Fourier coefficients of a linear Bloch wave and they exponentially localized at the lattice sites. One drawback to using actual Wannier functions is that (usually) there is no convenient analytical formulae and they must be computed numerically. Approximating the Bloch functions by the orbitals allows us to derive coefficients that depend directly on the physical parameters of waveguide system (8). Furthermore, they capture the appropriate band dynamics below.

The two lattices we consider in detail, Lieb and Kagome, are shown in Figs. 1 and 2, respectively. Both are nondimensionalized so that the distance between nearest neighbors is one. The lattice sites of the Lieb lattice are separated via the standard basis vectors

$$\mathbf{e}_1 = (1, 0), \quad \mathbf{e}_2 = (0, 1). \quad (14)$$

The nearest neighbor distances in the Kagome lattice are defined in terms of the vectors

$$\mathbf{v}_1 = \left(\frac{\sqrt{3}}{2}, \frac{1}{2}\right), \quad \mathbf{v}_2 = \left(\frac{\sqrt{3}}{2}, -\frac{1}{2}\right), \quad \mathbf{v}_3 = (0, 1). \quad (15)$$

As a result, the Lieb lattice sites used are given by the sets $\mathcal{R}_a = \{\mathbf{v}_{mn}^a \mid \mathbf{v}_{mn}^a = 2m\mathbf{e}_2 + (2n-1)\mathbf{e}_1\}$, $\mathcal{R}_b = \{\mathbf{v}_{mn}^b \mid \mathbf{v}_{mn}^b = 2m\mathbf{e}_2 + 2n\mathbf{e}_1\}$, $\mathcal{R}_c = \{\mathbf{v}_{mn}^c \mid \mathbf{v}_{mn}^c = (2m+1)\mathbf{e}_2 + 2n\mathbf{e}_1\}$ for $m, n \in \mathbb{Z}$. The Lieb (periodic) lattice vectors are $2\mathbf{e}_1$ and $2\mathbf{e}_2$.

In the case of the Kagome lattice the lattice points are located at $\mathcal{R}_a = \{\mathbf{v}_{mn}^a \mid \mathbf{v}_{mn}^a = (2m+1)\mathbf{v}_1 + 2n\mathbf{v}_2\}$, $\mathcal{R}_b = \{\mathbf{v}_{mn}^b \mid \mathbf{v}_{mn}^b = 2m\mathbf{v}_1 + 2n\mathbf{v}_2\}$, $\mathcal{R}_c = \{\mathbf{v}_{mn}^c \mid \mathbf{v}_{mn}^c = 2m\mathbf{v}_1 + (2n+1)\mathbf{v}_2\}$ where $m, n \in \mathbb{Z}$. The Kagome (periodic) lattice vectors are $2\mathbf{v}_1$ and $2\mathbf{v}_2$. To index the Kagome lattice we rewrite the labels in terms of the vectors $\mathbf{w}_1 = (0, 1)$ and $\mathbf{w}_2 = (\sqrt{3}, 0)$ which are related to the lattice vectors by the linear transformation: $2\mathbf{v}_1 = \mathbf{w}_1 + \mathbf{w}_2$ and $2\mathbf{v}_2 = \mathbf{w}_2 - \mathbf{w}_1$; hence we introduce the new labels $\tilde{m} = m - n$ and $\tilde{n} = m + n$ (the tilde notation is dropped after this point; so the equations for the Kagome lattice below are in the $\mathbf{w}_1, \mathbf{w}_2$ directions). Doing this makes it easier to find edge modes along the left or right edges. All points in the Lieb/Kagome lattices are obtained from translations of the lattice vectors beginning with three initial points.

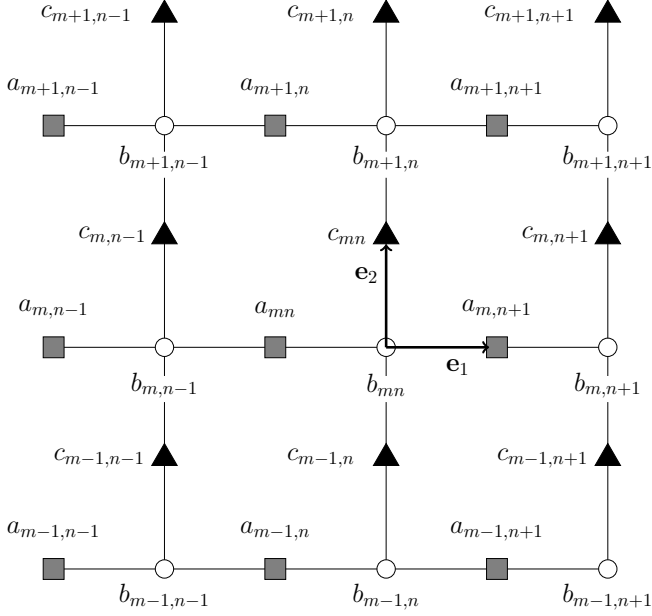


FIG. 1. The Lieb lattice consists of three interpenetrating square sublattices $V_a(\mathbf{r})$ (square site, \mathbf{a}), $V_b(\mathbf{r})$ (circle site, \mathbf{b}) and $V_c(\mathbf{r})$ (triangle site, \mathbf{c}). The vectors \mathbf{e}_1 and \mathbf{e}_2 are defined in (14). Lines denote nearest neighbor interactions. Shown is a bearded (straight) boundary condition on the left (right) edge.

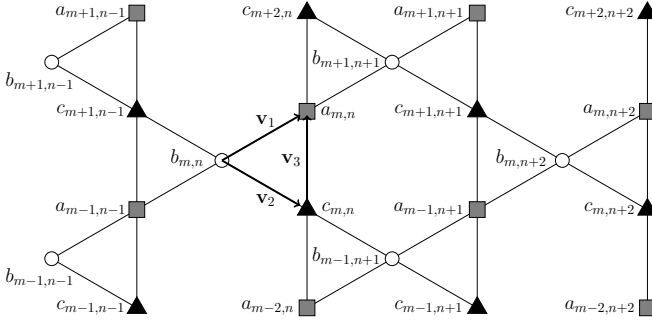


FIG. 2. The Kagome lattice consists of three interpenetrating triangular sublattices $V_a(\mathbf{r})$ (square sites, \mathbf{a}), $V_b(\mathbf{r})$ (circle sites, \mathbf{b}) and $V_c(\mathbf{r})$ (triangle sites, \mathbf{c}). The vectors \mathbf{v}_1 , \mathbf{v}_2 , and \mathbf{v}_3 are given in (15). Lines denote nearest neighbor interactions. Shown is a pointy (straight) boundary condition on the left (right) edge.

To leading order: in the Lieb lattice the b sites interact with both the nearest a and c sites, whereas the a, c sites only interact with the nearest b sites; in the Kagome lattice all nearest sites interact with the others. For experimental parameters used in [3] the coefficients in Eqs. (16)-(18) and (23)-(25) that represent nearest neighbor interaction are on the order of $\mathcal{O}(10^{-1})$, while the next-nearest neighbor coupling (not included) is on the order of $\mathcal{O}(10^{-3})$ for Lieb and $\mathcal{O}(10^{-5})$ for Kagome. For this reason, we only consider nearest neighbor overlap, but emphasize that longer range interactions could also be taken into account.

A. Lieb Tight-binding Approximation

Here we present a tight-binding model for the Lieb lattice. In deriving this set of equations only the dominant self and nearest neighbor interactions are taken into account. Since this is a leading order calculation we do not include any direct interaction between the a and c lattice sites (see Fig. 1) in our derivation. Weak on-site cubic nonlinearity is included in the equations. The semi-discrete system of coupled mode equations are given by

$$i \frac{da_{mn}}{dz} + (\Delta \mathbf{h}_{ab} \cdot \mathbf{A}_z + \gamma_{nl} |a_{mn}|^2) a_{mn} \quad (16)$$

$$+ \mathbb{L}_1^{ab}(z) b_{mn} + \mathbb{L}_{-1}^{ab}(z) b_{m,n-1} = 0,$$

$$i \frac{db_{mn}}{dz} + \gamma_{nl} |b_{mn}|^2 b_{mn} \quad (17)$$

$$+ \mathbb{L}_1^{ba}(z) a_{m,n+1} + \mathbb{L}_{-1}^{ba}(z) a_{mn}$$

$$+ \mathbb{L}_2^{bc}(z) c_{mn} + \mathbb{L}_{-2}^{bc}(z) c_{m-1,n} = 0,$$

$$i \frac{dc_{mn}}{dz} + (\Delta \mathbf{h}_{cb} \cdot \mathbf{A}_z + \gamma_{nl} |c_{mn}|^2) c_{mn} \quad (18)$$

$$+ \mathbb{L}_2^{cb}(z) b_{m+1,n} + \mathbb{L}_{-2}^{cb}(z) b_{mn} = 0,$$

such that $\mathbb{L}_{\pm\ell}^{ij}(z) = \mathbb{L}(\pm \mathbf{e}_\ell - \Delta \mathbf{h}_{ij}(z))$ and $\gamma_{nl} \geq 0$. The definitions of the coefficients \mathbb{L} and γ_{nl} , in terms of physical parameters, are given in Appendix A. Note that Eq. (17), unlike the other two equations, does not contain a linear coefficient depending on \mathbf{A}_z since $\Delta \mathbf{h}_{bb} = 0$.

We concentrate on edge modes that propagate along a semi-infinite strip. Outside this region the light beam is assumed to be negligibly small, hence we take zero boundary conditions on the left and right sides. Along the infinite m -direction we take large computational domains and implement periodic boundary conditions. For the lattice displayed in Fig. 1 we show two possible edge types: “bearded” (left) and “straight” (right). Any combination of these two edge types is possible e.g. straight-straight, straight-bearded, or bearded-bearded.

To find edge mode solutions localized along the left or right boundaries we look for solutions of the form

$$a_{mn}(z) = a_n(k_y; z) e^{i2mk_y},$$

$$b_{mn}(z) = b_n(k_y; z) e^{i2mk_y}, \quad (19)$$

$$c_{mn}(z) = c_n(k_y; z) e^{i2mk_y},$$

which reduce Eqs. (16)-(18) to

$$i \frac{da_n}{dz} + (\Delta \mathbf{h}_{ab} \cdot \mathbf{A}_z + \gamma_{nl} |a_n|^2) a_n \quad (20)$$

$$+ \mathbb{L}_1^{ab}(z) b_n + \mathbb{L}_{-1}^{ab}(z) b_{n-1} = 0,$$

$$i \frac{db_n}{dz} + \gamma_{nl} |b_n|^2 b_n \quad (21)$$

$$+ \mathbb{L}_1^{ba}(z) a_{n+1} + \mathbb{L}_{-1}^{ba}(z) a_n$$

$$+ \mathbb{L}_2^{bc}(z) c_n + \mathbb{L}_{-2}^{bc}(z) e^{-i2k_y} c_n = 0,$$

$$i\frac{dc_n}{dz} + (\Delta\mathbf{h}_{cb} \cdot \mathbf{A}_z + \gamma_{nl}|c_n|^2)c_n \quad (22)$$

$$+ \mathbb{L}_2^{cb}(z)e^{i2k_y}b_n + \mathbb{L}_{-2}^{cb}(z)b_n = 0 .$$

We solve Eqs. (20)-(22) with appropriate zero boundary conditions to obtain all Lieb lattice edge modes shown below.

B. Kagome Tight-binding Approximation

Next we give the tight-binding approximation for the Kagome lattice. As mentioned above, each lattice site interacts with two of the other nearest site types (e.g. a sites interact with nearest b and c sites). Similar to the Lieb case, we study a semi-infinite strip domain: zero boundary conditions on the left and right edges, and infinite boundary conditions along the m -direction. We focus on two types of boundary conditions: “pointy” (the analog of bearded for Lieb) and “straight” (see Fig. 2). Any combination of these two boundary types can be accommodated.

Taking into account self and nearest neighbor interactions and weak on-site nonlinearity we arrive at the following system of equations describing this Floquet lattice

$$i\frac{da_{mn}}{dz} + (\Delta\mathbf{h}_{ab} \cdot \mathbf{A}_z + \gamma_{nl}|a_{mn}|^2)a_{mn} \quad (23)$$

$$+ \mathbb{L}_1^{ab}(z)b_{m+1,n+1} + \mathbb{L}_{-1}^{ab}(z)b_{mn}$$

$$+ \mathbb{L}_3^{ac}(z)c_{m+2,n} + \mathbb{L}_{-3}^{ac}(z)c_{mn} = 0 ,$$

$$i\frac{db_{mn}}{dz} + \gamma_{nl}|b_{mn}|^2b_{mn} \quad (24)$$

$$+ \mathbb{L}_1^{ba}(z)a_{mn} + \mathbb{L}_{-1}^{ba}(z)a_{m-1,n-1}$$

$$+ \mathbb{L}_2^{bc}(z)c_{mn} + \mathbb{L}_{-2}^{bc}(z)c_{m+1,n-1} = 0 ,$$

$$i\frac{dc_{mn}}{dz} + (\Delta\mathbf{h}_{cb} \cdot \mathbf{A}_z + \gamma_{nl}|c_{mn}|^2)c_{mn} \quad (25)$$

$$+ \mathbb{L}_3^{ca}(z)a_{mn} + \mathbb{L}_{-3}^{ca}(z)a_{m-2,n}$$

$$+ \mathbb{L}_2^{cb}(z)b_{m-1,n+1} + \mathbb{L}_{-2}^{cb}(z)b_{mn} = 0 ,$$

where $\mathbb{L}_{\pm\ell}^{ij}(z) = \mathbb{L}(\pm\mathbf{v}_\ell - \Delta\mathbf{h}_{ij}(z))$. The coefficients \mathbb{L} and γ_{nl} are defined in Appendix A.

To find edge modes localized along the left or right boundaries, we consider solutions of the form

$$a_{mn}(z) = a_n(k_y; z)e^{imk_y} ,$$

$$b_{mn}(z) = b_n(k_y; z)e^{imk_y} , \quad (26)$$

$$c_{mn}(z) = c_n(k_y; z)e^{imk_y} ,$$

to obtain the reduced system of equations

$$i\frac{da_n}{dz} + (\Delta\mathbf{h}_{ab} \cdot \mathbf{A}_z + \gamma_{nl}|a_n|^2)a_n \quad (27)$$

$$+ \mathbb{L}_1^{ab}(z)e^{ik_y}b_{n+1} + \mathbb{L}_{-1}^{ab}(z)b_n$$

$$+ \mathbb{L}_3^{ac}(z)e^{i2k_y}c_n + \mathbb{L}_{-3}^{ac}(z)c_n = 0 ,$$

$$i\frac{db_n}{dz} + \gamma_{nl}|b_n|^2b_n \quad (28)$$

$$+ \mathbb{L}_1^{ba}(z)a_n + \mathbb{L}_{-1}^{ba}(z)e^{-ik_y}a_{n-1}$$

$$+ \mathbb{L}_2^{bc}(z)c_n + \mathbb{L}_{-2}^{bc}(z)e^{ik_y}c_{n-1} = 0 ,$$

$$i\frac{dc_n}{dz} + (\Delta\mathbf{h}_{cb} \cdot \mathbf{A}_z + \gamma_{nl}|c_n|^2)c_n \quad (29)$$

$$+ \mathbb{L}_3^{ca}(z)a_n + \mathbb{L}_{-3}^{ca}(z)e^{-i2k_y}a_n$$

$$+ \mathbb{L}_2^{cb}(z)e^{-ik_y}b_{n+1} + \mathbb{L}_{-2}^{cb}(z)b_n = 0 .$$

We solve Eqs. (27)-(29) with appropriate spatial boundary conditions to find all Kagome edge modes shown below.

III. LINEAR FLOQUET BANDS AND EDGE STATE DYNAMICS

We now compute linear ($\gamma_{nl} = 0$) edge states for the tight-binding systems given above. To accomplish this we compute the principal fundamental matrix for the reduced systems (20)-(22) or (27)-(29) after one period in z . From this we obtain the monodromy matrix at $z = T$ (where T is the helix pitch or period: $T = 2\pi/\Omega$, and $\Omega \equiv \Omega_b$). The eigenvalues of the monodromy matrix are the Floquet (characteristic) multipliers $\lambda(k_y)$. The Floquet exponents are computed, up to an additive constant, by

$$\alpha(k_y) = \frac{i \ln[\lambda(k_y)]}{T} + \frac{2\pi l}{T} , \quad l \in \mathbb{Z} . \quad (30)$$

Since the range of possible lattice rotation patterns is very large we focus our attention on driving patterns which have been shown to demonstrate interesting band structures in other lattice systems. Previous examples include in-phase rotation in honeycomb lattices [3], or π -phase offset among the sublattices that generate Weyl type-II points [6]. In particular we concentrate on the following driving patterns:

- same (in-phase) rotation

$$\mathbf{h}_j(z) = \eta(\cos(\Omega z), \sin(\Omega z)) , \quad (31)$$

- different radii, in-phase

$$\mathbf{h}_j(z) = R_j\eta(\cos(\Omega z), \sin(\Omega z)) , \quad R_j \leq 1 \quad (32)$$

- π -phase offset

$$\mathbf{h}_j(z) = \eta(\cos(\Omega z + \chi_j), \sin(\Omega z + \chi_j)) , \quad \chi_j = 0, \pi \quad (33)$$

- counter rotation

$$\mathbf{h}_j(z) = \eta(\cos(\Omega z), r_j \sin(\Omega z)) , \quad r_j = \pm 1 \quad (34)$$

- different frequency

$$\mathbf{h}_j(z) = \eta(\cos(l_j\Omega z), \sin(l_j\Omega z)) , \quad l_j \in \mathbb{N} , \quad (35)$$

- quasi one-dimensional motion

$$\mathbf{h}_j(z) = \eta (p_j \cos(\Omega z), q_j \sin(\Omega z)) , \quad (36)$$

$$p_j = 0 \text{ or } 1 , \quad p_j + q_j = 1 ,$$

where $j = a, b, c$, and $\eta \equiv \eta_b$. We point out that each of the driving functions above have period T i.e. $\mathbf{h}_j(z+T) = \mathbf{h}_j(z)$, where $T = 2\pi/\Omega$ and do not affect the translation symmetry (periodicity in \mathbf{r}). The reason is that each individual sublattice maintains a periodic spatial structure (square for Lieb, triangular for Kagome), and since the potential (2) is simply the sum of these sublattices, it too must preserve translation invariance.

For all examples considered in this paper we use lattice depth $V_0^2 = 45$ and angular frequency $\Omega = 2\pi/1.5$; this corresponds a helix pitch of $T = 1.5$. These parameters are taken to model the experimental parameters reported in [3].

A. Lieb Floquet bands

In this section we compute the Floquet bands and location of edge modes for the Lieb lattice. These bands, defined in Eq. (30), are calculated for the linear ($\gamma_{nl} = 0$) system of equations given in Eqs. (20)-(22). The band structures consist of bulk or extended modes (indicated by solid black regions) and gapless edge or localized modes (indicated by curves, highlighted with color).

In the absence of helical driving ($\eta = 0$) the Lieb dispersion bands are known to possess a flat band that spans the Brillouin zone cf. [22]. Regardless of the left/right boundary conditions (e.g. bearded/bearded, bearded/straight, or straight/straight) the band diagram resembles that shown in Fig. 3. Though not visible, within the green colored flat band region there exist both bulk modes *and* localized edge modes. Flat band edge modes are found to exist in the neighborhood of both edge types.

The first case with driving is that of same rotation (31) among the waveguides. Several typical Floquet bands are shown in Fig. 4 for different boundary conditions. Each case contains traveling ($\alpha'(k_y) \neq 0$) and stationary ($\alpha'(k_y) = 0$) modes; at least one of each type on both sides (left and right). Again, since it is not visible, we also point out that at the flat band there are both bulk and edge modes.

Each boundary type is found to exhibit a distinct signature in its band structure. For instance, the Floquet bands on the straight edge possess a steep slope (large group velocity), particularly near $k_y = \pi/2$, whereas the bearded edge modes have a shallow slope (smaller group velocity) throughout the Brillouin zone. As a consequence, for this rotation pattern there are fast edges (straight) and slow edges (bearded).

To establish these are indeed topologically protected edge modes we also calculate the Chern number for each bulk band. The definition and computation of the Chern number is described in Appendix B. The Bulk-edge correspondence states that the Chern numbers in both the

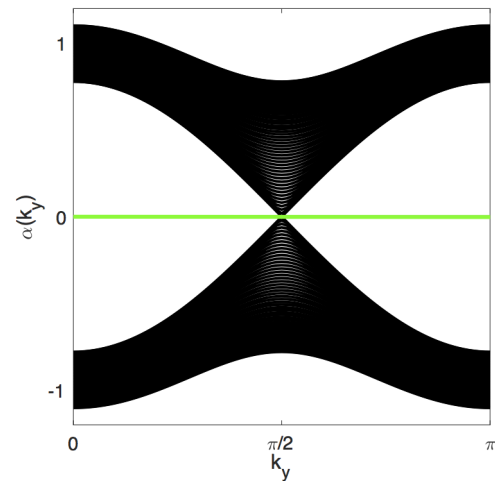


FIG. 3. (Color online) Lieb Floquet bands with no lattice driving. Green curve indicates that flat band modes are located on/near both edges. The parameters used are: $\eta = 0, \sigma_x = \sigma_y = 0.3$.

bulk and edge problems are the same [30]. Furthermore, the Chern number is equal to the net number of chiral edge modes above the band minus the number below the band [31, 32]. A corollary of this is that the Chern number is independent of the boundary used; hence for a set of bulk bands with different Chern numbers (see below) there will be a gapless edge state; even in the presence of a lattice defect. The nontrivial Chern number in the top and bottom spectral bands of Fig. 4 indicates the presence of topological edge states. Since the flat band has the same number of chiral modes above and below, its Chern number is zero. This figure also highlights that the spectral bulk bands are *unaffected* by the boundary conditions.

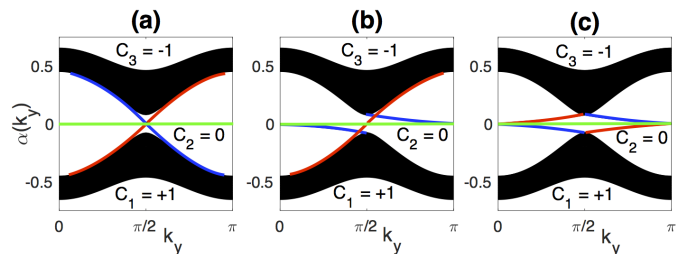


FIG. 4. (Color online) Lieb Floquet bands for same phase lattice driving (31) with different boundary conditions. The boundary condition on the left [right] edge is: (a) straight [straight], (b) bearded [straight], and (c) bearded [bearded]. Red curves indicate edge modes on right edge, blue curves denote left edge modes, and the green curves designate flat band modes on both edges. The parameters used are: $\eta = 2/3, \sigma_x = \sigma_y = 0.3$. Chern numbers for each bulk band are included.

For all remaining band calculations we use the boundary combination shown in Fig. 1, namely bearded on the left and straight on the right. The next case considered is that of π -offset rotation (33). The corresponding

Floquet bands are displayed in Fig. 5 for three different values of η i.e. radii. Each case contains a set of topologically protected edge states residing in the central gaps. One significant difference between these bands and those found in Fig. 4(b) is the absence of any flat band modes. In addition, at a certain radius threshold [see Fig. 5(b)] the gap between different branches of the Floquet exponent (30) closes and the system undergoes a topological transition. Since it is not possible to distinguish between different bulk bands at this transition point, we do not calculate Chern numbers in Fig. 5(b).

Increasing the helix radius beyond this threshold spawns an entirely new family of edge states located near the edge of the Floquet region: $\alpha_{\text{edge}} = \pm\pi/T$. Since now there is one chiral mode above and below each bulk band, the Chern number is zero. Finally, we point out that the bearded edge modes shown in Fig. 5 move considerably faster than those in Fig. 4(b). Hence it is possible, (by changing the lattice rotation pattern) to support faster edge mode propagation along a bearded edge.

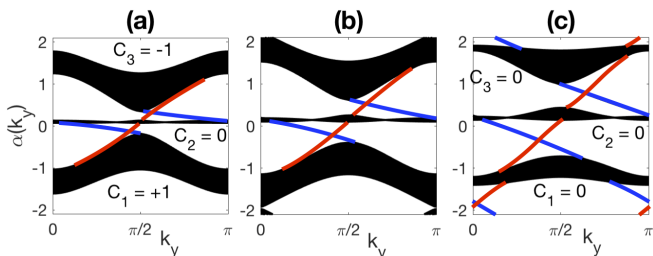


FIG. 5. (Color online) Lieb Floquet bands for π -offset rotation (33). The boundary condition on the left [right] edge is bearded [straight]. Red curves indicate edge modes on right edge, blue curves denote left edge modes. The parameters used are: (a) $\eta = 1.4/15$, (b) $\eta = 1.8/15$, and (c) $\eta = 2.2/15$ with $\chi_a = \chi_c = \pi$, $\chi_b = 0$, $\sigma_x = \sigma_y = 0.3$.

Many other lattice rotation patterns are also found to support topologically protected edge states. In Fig. 6 we show Floquet bands for various driving patterns on the Lieb lattice. The dispersion curves corresponding to same rotation driving (31) with elliptical ($\sigma_x \neq \sigma_y$), rather than circular, waveguides are shown in Figs. 6(a) and 6(b). In the former case ($\sigma_x < \sigma_y$) the major axis of the ellipse is parallel to the m -direction, while in the latter scenario ($\sigma_x > \sigma_y$) the major axis is parallel to the n -direction. Doing this is found to either squeeze [see Fig. 6(a)] or stretch [see Fig. 6(b)] the width of the upper and lower bulk bands. We find that this lattice rotation arrangement does support both extended (bulk) and localized (edge) flat band modes, both at $\alpha(k_y) = 0$.

Next we consider when the sublattices are rotating in-phase with each other, but with different radii (32). Examining the corresponding band structure in Fig. 6(c) we observe the presence of unidirectional modes and the absence of any flat band states. The next set of bands [see Fig. 6(d)] correspond to different frequency (35) among the sublattices. In particular we examine when the a and c lattice sites rotate at twice the frequency of the b sites. Overall, the band and Chern structure resembles

that of the same rotation case shown in Fig. 4(b) without, however, the presence of any flat band modes. The bands corresponding to counter rotation (34) are shown in Fig. 6(e). For these parameters the b sites are rotating in a counter-clockwise fashion while the a and c sites move in the clockwise direction. No localized modes are found for these parameters, and only trivial Chern numbers are found.

The final case is that of quasi one-dimensional motion (36) where each sublattice moves in only one direction, either the m or n direction. We consider a scenario in which the a and c sites oscillate only in the m -direction ($p_a = p_c = 0, q_a = q_c = 1$), while the b sites oscillate only in the n -direction ($p_b = 1, q_b = 0$). The corresponding bands are shown in Fig. 6(f). For this relatively simple lattice motion we identify the presence unidirectional traveling edge modes. Looking closer we note that these modes travel in an orientation opposite those found in previous cases i.e. they possess opposite chirality. In contrast to the previous cases, here the straight (right) edge modes move in the negative direction ($\alpha'(k_y) < 0$), while bearded (left) edge modes travel in the positive direction ($\alpha'(k_y) > 0$). This is reflected in the Chern numbers of the upper and lower bulk bands which have opposite signs compared to the previous cases. No flat band modes are found.

B. Lieb edge mode dynamics

In this section we present mode evolutions for some the edge states found above. Specifically, we integrate the full Lieb tight-binding coupled mode system (16)-(18) for an edge mode with a localized envelope in m . The initial conditions taken are

$$\begin{aligned} a_{mn}(0) &= \text{sech}(\mu m) a_n(k_y) e^{i2mk_y}, \\ b_{mn}(0) &= \text{sech}(\mu m) b_n(k_y) e^{i2mk_y}, \\ c_{mn}(0) &= \text{sech}(\mu m) c_n(k_y) e^{i2mk_y}, \end{aligned} \quad (37)$$

using a typical value $\mu = 0.1$. The exponentially decaying edge eigenmodes $a_n(k_y)$, $b_n(k_y)$, and $c_n(k_y)$ are obtained directly from solving system (20)-(22) at a chosen k_y . In all cases the eigenmode two-norm is fixed to one i.e. $\sum_n (|a_n|^2 + |b_n|^2 + |c_n|^2) = 1$. We take periodic boundary conditions in m (top/bottom edges) and bearded-straight zero boundary conditions in n . The left-most lattice site is located at $n = 0$, while the right-most site is $n = N$, where N is taken to be large $\sim O(100)$. The system is integrated using a fourth-order Runge-Kutta method.

The z -dynamics for several edge mode profiles are presented in Fig. 7. For simplicity of presentation, we only show the most dominant (largest magnitude) sublattice mode (e.g. the c -mode tends to be considerably larger than the a -mode near the straight side). The evolutions shown in Figs. 7(a-d) correspond to same rotation among the three sublattices, the Floquet bands of which are shown in Fig. 4(b). The two topological traveling

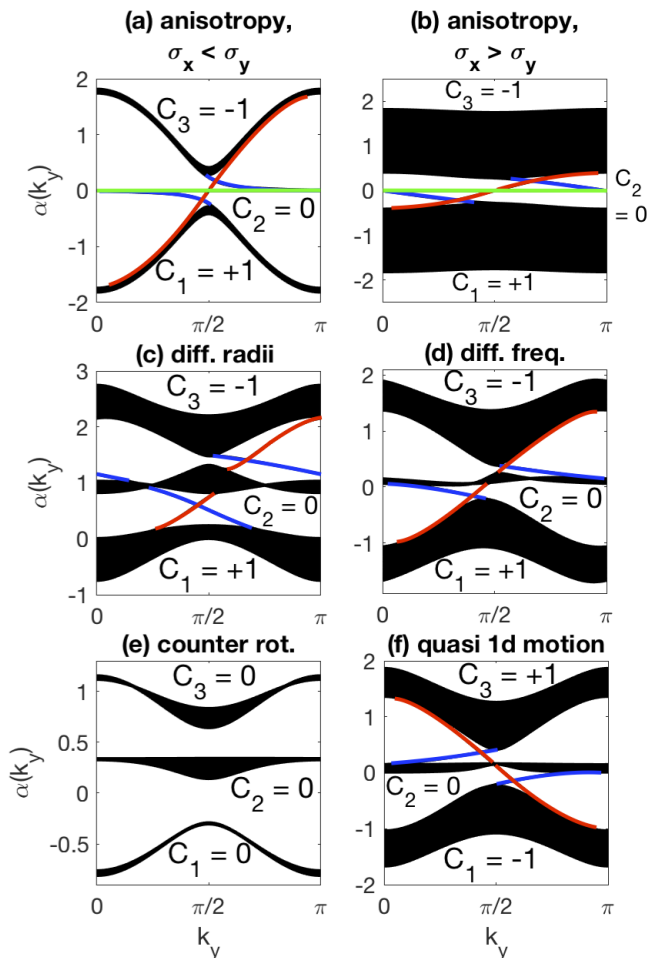


FIG. 6. (Color online) Lieb Floquet bands for various rotation patterns. The boundary condition on the left [right] edge is bearded [straight]. Red curves indicate edge modes on right edge, blue curves denote left edge modes, and the green curves designate flat band modes on both edges. The parameters used are: (a-b) $\eta = 2/3$, (c) $\eta = 2/3, R_a = R_c = 3/5, R_b = 1$, (d) $\eta = 2.2/15, l_a = l_c = 2, l_b = 1$, (e) $\eta = 3/15, r_a = r_c = -1, r_b = 1$, (f) $\eta = 3/15, p_a = p_c = 0, p_b = 1$; with $\sigma_x = \sigma_y = 0.3$ in all except (a) $\sigma_x = 0.3, \sigma_y = 0.5$ and (b) $\sigma_x = 0.5, \sigma_y = 0.3$. Chern numbers for each bulk band are included.

modes ($\alpha'(k_y) \neq 0$) are observed to propagate with constant velocity in either the negative (on the left side) [see Fig. 7(a)] or positive (on the right side) direction [see Fig. 7(b)]. As expected, the mode on the bearded edge travels considerably slower than the straight edge mode. In order to get a well-localized edge mode the value of $\alpha(k_y)$ must be chosen well-separated from the bulk bands. This is why the same rotation mode shown in Fig. 7(a) has a different mode number k_y than the others. When an edge mode with a corresponding Floquet exponent located near a bulk band is used the mode is found to *not* maintain its well-localized structure over long distances and will *not* propagate through lattice defects. In a sense such modes can be considered to be quasi-bulk bands. This is discussed in Sec. IV.

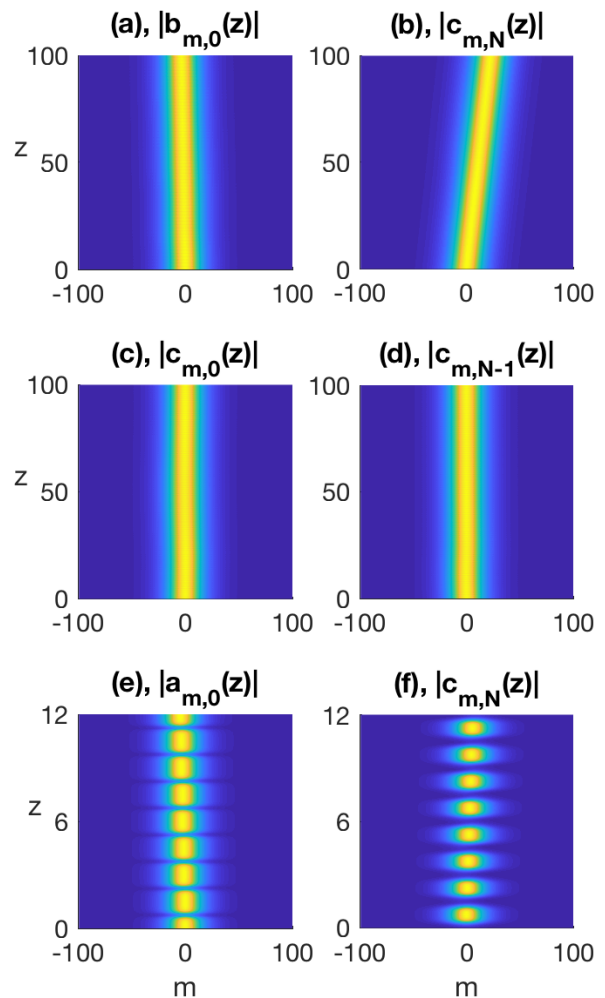


FIG. 7. Evolution of edge profile in the Lieb lattice. The edge modes shown in panels (a-d) correspond to the Floquet bands in Fig. 4(b) at: $(k_y, \alpha) =$ (a) $(1.8, .0628)$, (b) $(1.65, .0362)$, (c-d) $(1.65, 0)$. The edge states in panels (e-f) correspond to the bands shown in Fig. 5(c) at $(k_y, \alpha) =$ (e) $(.2, -1.94)$ and (f) $(.2, -1.68)$.

Next we evolve the stationary flat band states in Fig. 4(b). When solving for the Floquet exponent on the straight edge the numerical algorithm we use produces two stationary modes: one with $|\alpha(1.65)| = O(10^{-4})$ and another at $|\alpha(1.65)| = O(10^{-11})$. In Fig. 7 we only consider the latter mode whose magnitude is smaller. We note that the magnitude of these flat band modes is found to peak not along the boundary, but instead at an interior column (at $n = N - 1$ on the right). The flat band evolutions are shown in Figs. 7(c-d). As expected, these modes do not move from their initial position.

The final set of evolutions we present is that of π -offset rotation. We omit the edge mode dynamics for the bands shown in Fig. 6, but note that many similar evolution patterns are observed in those cases as well. We focus on the π -offset modes near the Floquet edge in Fig. 5(c). The corresponding mode evolutions are displayed in Figs. 7(e-f). The mode profiles on both sides are

observed to oscillate with the same period as the lattice driving ($T = 1.5$). Moreover along the bearded edge [see Fig. 7(e)] energy fluctuates back-and-forth between the a/c sites (in-phase with each other) and the b -sites (out-of-phase). If the overall beam (13) is wide this oscillatory behavior may be difficult to detect. However, along the $n = 0$ column there should be a noticeable oscillation in the beam intensity. In Fig. 7(f) the straight edge mode shown, $c_{m,N}$, has a similar, but out-of-phase, evolution pattern with the b -sites; meanwhile the a lattice modes are relatively small in comparison.

C. Kagome Floquet bands

In this section we compute Floquet bands for the Kagome lattice. The dispersion curves are computed in the same way as the Lieb bands in the previous section, via the Floquet exponents (30), for the rotation patterns listed in Eqs. (31)-(36). All bands are computed from the one-dimensional tight-binding system given in Eqs. (27)-(29).

Before considering a driven case we first examine the dispersion bands for stationary waveguides ($\eta = 0$). The Floquet bands for different boundary conditions are displayed in Fig. 8, where both traveling and non-traveling edge states are observed. Regardless of the edge type we find a flat top band. By introducing a pointy edge (see Fig. 2) we observe a “vine” type family of edge modes which do not span the gap. To our knowledge flat band *edge* modes have not previously been considered in the context of a kagome photonic lattice waveguide. Interestingly, below we do not find any flat bands like these in the presence of periodic driving (unlike the Lieb lattice above).

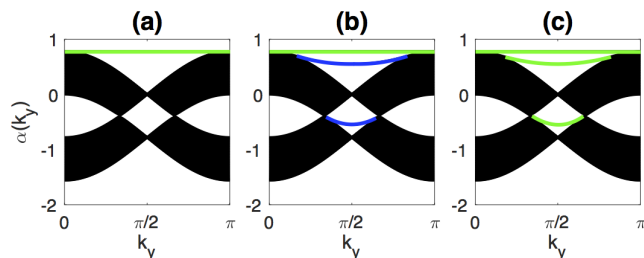


FIG. 8. (Color online) Kagome Floquet bands in the absence of rotation with different boundary conditions. The boundary condition on the left [right] edge is: (a) straight [straight], (b) pointy [straight], and (c) pointy [pointy]. Blue curves denote left edge modes and the green curves designate modes on both edges. The parameters used are: $\eta = 0$, $\sigma_x = \sigma_y = 0.3$.

The first driven case to consider is that of same rotation among all sublattices (31). The corresponding band diagrams are shown in Fig. 9 for three different boundary combinations. Also included are the corresponding Chern numbers of the bulk bands. Here and below we highlight with color only the (topological) gapless edge modes. Similar to the Lieb lattice above, here we observe

that different boundary conditions carry distinguishable edge band structure. Both edge types possess a topological edge mode in the central gap ($-0.5 \leq \alpha(k_y) \leq 0$). These gapless modes have sign-definite group velocity (unidirectionality) throughout the gap. For the straight edge there are edge modes near $\alpha = 0.5$ that span a very small gap between the middle at top bulk bands. To see that the mode actually crosses the gap one must zoom in very close. On the other hand, when a pointy edge is introduced we observe the “vine” type curve in the upper gap ($0.3 \leq \alpha(k_y) \leq 0.4$). In either case the bands in the upper gap do span the entire gap (and so they are highlighted with color). We point out that the pointy “vine” edge curves are not slope-definite, in other words depending on k_y the group velocity may be either positive ($\alpha'(k_y) > 0$) or negative ($\alpha'(k_y) < 0$). Also, while the top bulk band looks flat, it is not. This is different than the Lieb lattice in Fig. 4 where there is a flat band at $\alpha = 0$.

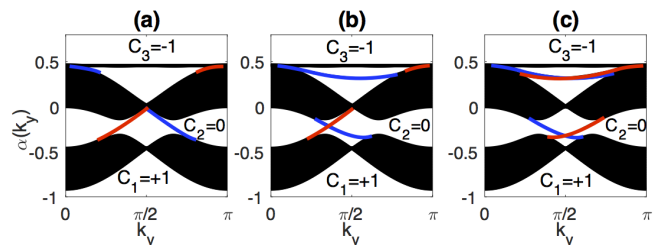


FIG. 9. (Color online) Kagome Floquet bands for same phase lattice rotation (31) with different boundary conditions. The boundary condition on the left [right] edge is: (a) straight [straight], (b) pointy [straight], and (c) pointy [pointy]. Red curves indicate edge modes on right edge, blue curves denote left edge modes. The parameters used are: $\eta = 2/3$, $\sigma_x = \sigma_y = 0.3$. Chern numbers for each bulk band are included.

For the remaining Kagome band diagrams we consider pointy-straight boundary conditions, similar to those in Fig. 2. When the individual waveguides are elliptical in shape (major axis parallel to the n -direction, $\sigma_x > \sigma_y$) and all sublattices are rotating in-phase with each other (31), we find the band diagram shown in Fig. 10(a). While these bands have the same Chern structure as those found in Fig. 9(b), this band structure bears little resemblance to the isotropic case. The pointy edge (blue) bands are observed to have slopes of positive or negative sign indicating that the system admits modes that may travel in either direction. We categorize this mode as topological since it spans the gap and corresponds to a nontrivial Chern number; even though it is not unidirectional throughout the entire gap. Moreover, if we evolve a mode frequency at a frequency α that does not support any other bulk or edge modes, we do observe unidirectional motion. Additionally, there is a set of topological modes located on the straight edge that span the central gaps.

We next examine different radii among the sublattices (32). In particular we consider when the a and c sublattices have smaller radii ($R_a = R_c = 0.6$) com-

pared to the b lattice sites ($R_b = 1$). The corresponding band diagram is shown in Fig. 10(b). Numerous gapless modes on both edges are found; all in agreement with the Chern numbers. One unusual family of edge states is located on the straight edge and have sign-indefinite group velocity, yet still span the gap [see minimum point near $(k_y, \alpha) = (1.7, 1.4)$]. Indeed, when an envelope was formed nearby this point and propagated into a defect barrier it did backscatter.

The Floquet bands corresponding to different frequency among the sublattices –see: Eq. (35)– are shown in Fig. 10(c). Here we take the a and c sublattices to oscillate twice as fast as the b sites. Both interior gaps contain topological modes that span their respective gaps. In the upper gap there is an additional non-topological band (colored in black) which does not span the gap, and hence does not affect the Chern invariant. The pointy edge band in the upper gap (colored in blue) has a small negative slope.

When a π -phase offset (33) is introduced between the sublattices a threshold phenomena, similar to that observed in Fig. 5 for the Lieb lattice, is found to occur. Increasing the lattice driving (helix radius) we observe the gap between adjacent Floquet exponent bands (30) close at some threshold value $\eta_T > 0$ and then reopen with a new family of edge states for $\eta > \eta_T$. In Fig. 10(d) we show the bands above this threshold; here we see numerous gapless modes on both edges. Since the net number of chiral modes above and below the spectral bands are the same, the resulting Chern number is zero for each.

Counter rotation among the sublattices (34), specifically when the a and c lattice sites have the opposite orientation to that of the b sites, is considered next. The corresponding bands are shown in 10(e). In contrast to the Lieb lattice above [see Fig. 6(e)], here we *do* find some edge waves. Both Floquet bands in the upper gap have slope that is sign-definite, meanwhile the pointy (left) edge mode in the lower gap has a small strip where there are both negative and positive directional modes.

The final scenario we investigate is that of the quasi one-dimensional rotation pattern (36). A band diagram for this arrangement is shown in Fig. 10(f). The a and c lattice sites only move in the m -direction ($p_a = p_c = 0$), while the b sites only move in the n -direction ($q_b = 0$). Relative to several previous cases, these edge modes tend to move in a clockwise (as opposed to counter-clockwise) fashion. As a result, the gap modes have opposite chirality and the corresponding Chern number have opposite sign from those found in the previous rotation patterns.

It is worth mentioning some of the similarities between the Lieb and Kagome lattices. Gapless edge states are found for same sublattice rotation (31) in both cases. Introducing a π -offset (33) among the sublattices introduces a threshold point in η where adjacent Floquet bands touch (see Fig. 5) and reopen with new gapless edge modes near the Floquet edges $\alpha_{edge} = \pm\pi/T$. Consequently, the Chern numbers are all zero and resemble those observed in [32] and [6]. The quasi one-dimensional rotation pattern equation (36)–see Fig.(10)(f) is found to

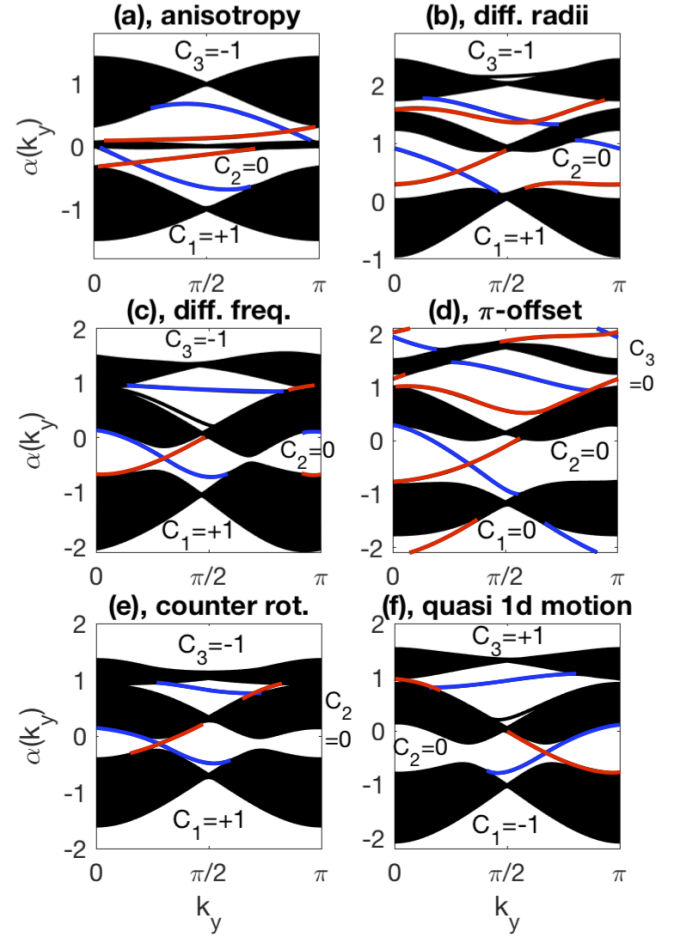


FIG. 10. (Color online) Kagome Floquet bands for various rotation patterns. The boundary conditions on the left [right] edge is pointy [straight]. Red curves indicate gapless edge modes on right edge, blue curves denote gapless left edge modes. The parameters used are: (a) $\eta = 2/3$, (b) $\eta = 2/3, R_a = R_c = 3/5, R_b = 1$, (c) $\eta = 2.2/15, l_a = l_c = 2, l_b = 1$, (d) $\eta = 2.2/15, \chi_a = \chi_c = \pi, \chi_b = 0$, (e) $\eta = 1/5, r_a = r_c = -1, r_b = 1$, (f) $\eta = 1/5, p_a = p_c = 0, p_b = 1; \sigma_x = \sigma_y = 0.3$. in all except (a) where $\sigma_x = 0.5, \sigma_y = 0.2$. Chern numbers for each bulk band are included.

reverse the direction modes propagate as well as the sign of the Chern invariants.

To further highlight these similarities among similar rotation patterns, in Appendix C we have included the Floquet bands for the honeycomb (see Fig. 16) and staggered square (see Fig. 17) lattices for rotation patterns and parameters similar those considered above. Their bands are found to exhibit similar structure in response to similar driving patterns. This highlights that lattice driving, or combinations thereof, could be tailored to suit the need of potential future applications involving these topologically protected modes.

D. Kagome edge mode dynamics

In this section we provide evolution dynamics for several Kagome edge modes found in the previous section. We integrate Eqs. (23)-(25) using the initial conditions

$$\begin{aligned} a_{mn}(0) &= \text{sech}(\mu m) a_n(k_y) e^{imk_y}, \\ b_{mn}(0) &= \text{sech}(\mu m) b_n(k_y) e^{imk_y}, \\ c_{mn}(0) &= \text{sech}(\mu m) c_n(k_y) e^{imk_y}, \end{aligned} \quad (38)$$

for the edge modes a_n, b_n, c_n found by numerically solving system (27)-(29) at a particular k_y . As with the Lieb lattice, we fix $\sum_n (|a_n|^2 + |b_n|^2 + |c_n|^2) = 1$. A slowly-varying sech envelope is attached in the m -direction with $\mu = 0.1$. Here we only show the most dominant sublattice edge mode profile either on the left (pointy edge) at $n = 0$, or the right (straight edge) at $n = N \gg 1$.

Some evolution patterns are shown in Fig. 11. The first case considered is that of same rotation among all sublattices (31) with corresponding Floquet bands shown in Fig. 9(b). Each gap has topologically protected edge modes on both sides, and each propagates with constant velocity. By attaching a slowly-varying envelope along the edge initially (38) we typically excite just the desired mode k_y and a small sideband. When the spatial envelope is too narrow we find that many additional frequencies, such as those that support bulk modes, can be excited.

The evolutions in Figs. 11(a) and (c) are both located along the pointy edge and evolve at a constant negative velocity. The majority of the energy resides in the outermost column of lattice sites, located at $b_{m,0}$, hence we display the b -mode profiles. Conversely, along the straight edge [see Figs. 11(b) and (d)] the gapless modes propagate in the positive direction and most of the energy is shared between the a and c sites; we only show the c -sublattice mode dynamics.

The evolution of a Kagome lattice with a π -phase offset between the b sites and the a, c lattice sites (33) is shown in Figs. 11(e-f). The corresponding dispersion curves are displayed in Fig. 10(d). The evolution dynamics here resemble those of the Lieb lattice [see Fig. 7(e-f)], as well as those seen in honeycomb and staggered square [7] when the sublattices are out of phase with each other. In both cases shown here, the modes are found to oscillate back-and-forth between the a/c and b lattice sites over the course of one lattice period ($T = 1.5$) and propagate with the group velocity.

IV. DEFECT BARRIER

Edge states associated with other cf.[2, 3, 7] helically driven photonic lattices have been shown to exhibit robust scatter-free motion in the presence of lattice defects. Here we introduce a lattice defect barrier and monitor the mode evolution as it encounters this barrier. Physically, the defects we consider correspond to the absence of lattice site waveguides. As such, there is little beam

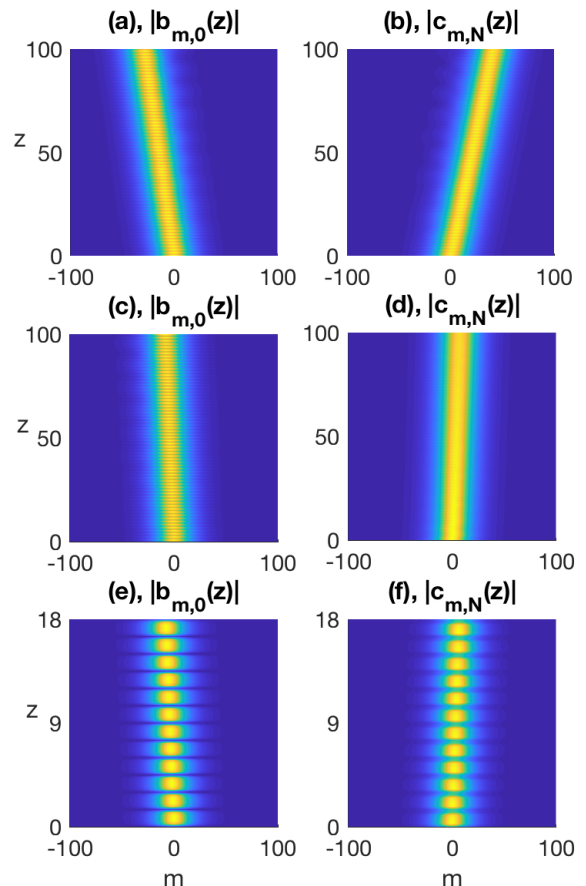


FIG. 11. Evolution of edge profile in the Kagome lattice. The edge modes shown in panels (a-d) correspond to the Floquet bands in Fig. 9(b) with Floquet exponents: (a) $\alpha(1.2) = -.231$, (b) $\alpha(1.2) = -.178$, (c) $\alpha(1.2) = .343$, (d) $\alpha(3) = .453$. The edge states in panels (e-f) correspond to the bands shown in Fig. 10(d) at $k_y = 0.2$ where $\alpha =$ (e) 1.84 and (f) 2.04.

propagation in these areas and so we set the beam field to be zero there.

A. Linear Evolution

First, consider the linear Lieb lattice with same rotation waveguide motion; the Floquet bands of which are shown in Fig. 4(b). We evolve an edge state into a defect barrier located in the region $(m, n) \in [-30, -27] \times [0, 2]$ along the bearded edge, and $(m, n) \in [27, 30] \times [N-2, N]$ for a, b sites and $[26, 30] \times [N-2, N]$ for c sites along the straight edge. Put another way, the wave field is set to zero for every lattice site inside these regions. In the absence of a barrier, the mode profile evolution along the straight edge is shown in Fig. 7(b). Several snapshots of a topologically protected mode are displayed in the right column of Fig. 12. All intensity plots given here (and below) are taken relative to the first snapshot in the series. The topologically protected mode encounters the lattice defect and we see that it propagates around the barrier;

there is no backscatter. We note that in several of our simulations if the mode envelope (37) is too narrow i.e. μ not sufficiently small, then modes outside the band gap can be excited and noticeable deterioration of the edge state occurs.

An example of a Lieb mode evolving through a defect along the bearded edge is shown in the left column of Fig. 12. The rotation pattern used is that of π -offset among the sublattices (33) whose corresponding band diagram is given in Fig. 5(c). In the absence of defect, the mode propagation is shown in Fig. 7(e). The reason we choose to show a mode with this rotation pattern, and not same rotation, is because the group velocity is much larger [cf. Fig. 4(b)], and we do not have to wait as long for the mode to evolve. Here the edge state is found to also pass scatter-free through the defect.

We point out an interesting mode-defect interaction in the case of same sublattice rotation (31) when the Floquet exponent [see Fig. 4(b)] is not well separated from the bulk bands. The evolution of a mode along the straight edge corresponding to a Floquet exponent deep within the band gap was displayed in Fig. 12 (right column). When we instead consider a mode, on the same Floquet edge band, whose position in the band diagram is nearby a bulk band we observe significant deterioration of the edge state. In Fig. 13, for a mode whose value $\alpha(k_y)$ lies nearby the bulk modes, a significant portion is observed to disperse away from the defect barrier and diminish in intensity. We point out that this occurs despite the topological protection. This mode appears to experience some transfer/leakage of energy into extended bulk states. Topologically protected modes whose Floquet exponents are located deep in the gap (well away from the bulk) appear to avoid this effect.

The mode evolutions for the Kagome lattice in the presence of a defect barrier are considered next. The defect along the pointy edge lies in the region $0 \leq n \leq 3$, and $N - 3 \leq n \leq N$ along the straight edge, with $-1 \leq m \leq 2$ for b and c lattice sites and $-2 \leq m \leq 1$ for a sites. Two intriguing cases are presented. The first is that of an edge mode propagating along a straight edge, the corresponding unidirectional band diagram is shown in Fig. 9(b). In the absence of a barrier the mode propagation is displayed in Fig. 11(b). The mode evolution with defect is presented in the right column of Fig. 14. The topologically protected edge state works its way around the defect and exits with the intensity it entered with.

The next case we examine has an edge mode with corresponding dispersion curve that is *not* unidirectional throughout the Brillouin zone, yet still crosses a band gap; i.e. a topological mode with group velocity that changes sign. Consider the pointy edge mode located at $(k_y, \alpha) = (1.2, 0.343)$ in Fig. 9(b); to the left of the minimum. This band has two different slope velocities signs depending on k_y . In the absence of defect, the constant velocity mode propagation is presented in Fig. 11(c). With defect, the mode evolution is shown in the left column of Fig. 14. Here the mode travels to-

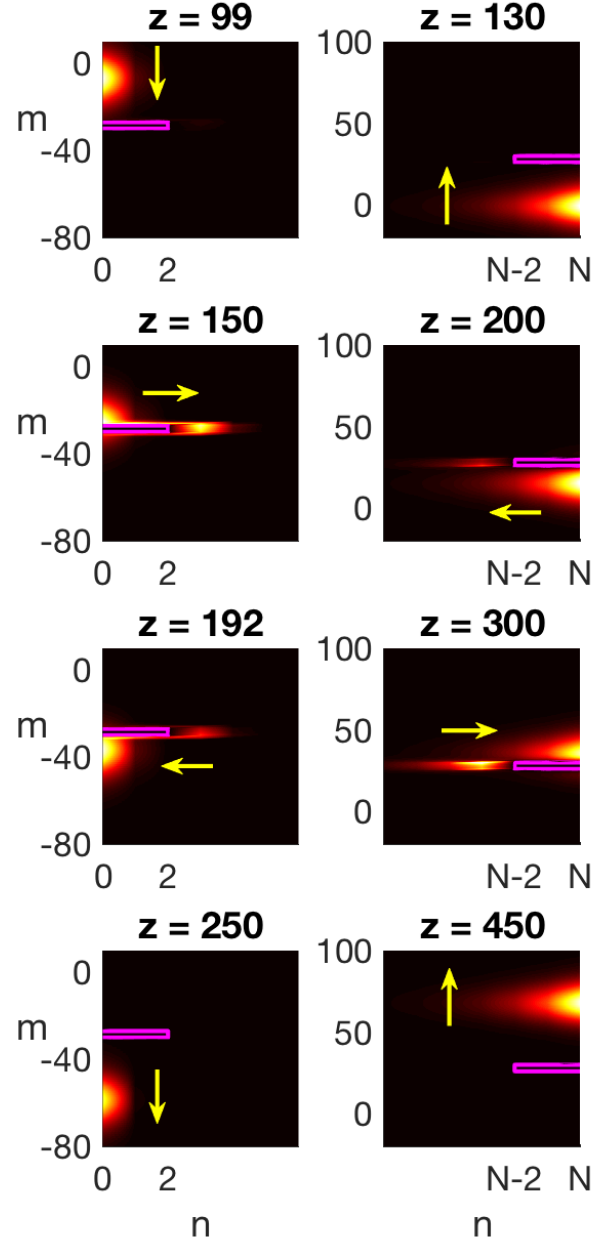


FIG. 12. Linear topologically protected edge mode dynamics encountering a defect barrier in the Lieb lattice. (Left column) Intensity evolution $|a_{mn}(z)|^2$ along bearded edge with π -offset rotation corresponding to the Floquet bands in Fig. 5(c) and $(k_y, \alpha) = (0.2, -1.94)$. (Right column) Intensity evolution $|c_{mn}(z)|^2$ along straight edge for same rotation corresponding to the Floquet bands in Fig. 4(b) with $(k_y, \alpha) = (1.65, .0362)$.

wards the barrier, but instead of passing around the defect barrier, it ceases movement in the negative direction and scatters backward with a noticeable loss in intensity. This backscattering tends to occur when there are other modes, bulk or edge, at the same frequency α that can become excited at the defect. This was also the case for the mode shown in Fig. 13.

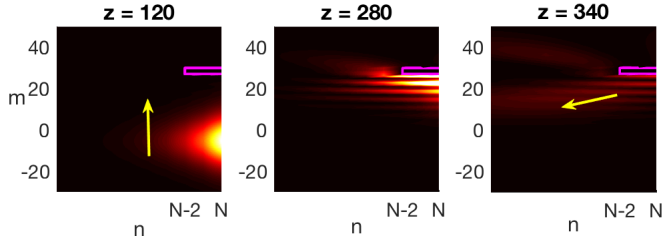


FIG. 13. Linear edge mode dynamics encountering a defect barrier in the Lieb lattice with the Floquet band positioned close to the bulk. Intensity evolution $|c_{mn}(z)|^2$ along straight edge for same rotation corresponding to the Floquet bands in Fig. 4(b) at $\alpha(2) = .191$.

B. Nonlinear Evolution

In this final section we consider nonlinear modes ($\gamma_{nl} \neq 0$) in the presence of lattice defects. For weak nonlinearity, with parameters similar to those considered above, nonlinear modes in honeycomb lattice have been found to exist when there is longitudinal driving [7, 18]. There it was found that the edge solitons ‘inherited’ the topological protection from the linear mode; we look to see if that is also the case here.

To begin, we note that there is a small parameter that is related to the relatively rapid driving frequency $\epsilon = 1/\Omega \approx 0.239$. The weak nonlinearity coefficient is set to $\gamma_{nl} = \epsilon$. We next look for a soliton mode, which is a balance between dispersion and self-focusing nonlinearity. As such, we initialize these modes similar to (37) and (38) except we add an amplitude coefficient A in front of the hyperbolic secant terms that satisfy the balance $A^2\gamma_{nl} = \mu^2|\alpha''(k_y)|$. The full *nonlinear* Lieb (16)-(18) and Kagome (23)-(25) systems are then evolved in z .

In Fig. 15 we show two nonlinear topologically protected solitons: one with in Lieb lattice and and the other Kagome, using the same parameters taken in Figs. 12 and 14 along the straight edge. Taking the balance given above, the nonlinear modes are found to closely mirror the unidirectional behavior of the linear states. Namely, for edge modes whose Floquet exponent is deep in the gap and slope-definite throughout the gap we observe scatter-free propagation around the defect. When the mode is not sufficiently deep in the gap or the sign of the group velocity depends on k_y , then the nonlinear mode can exhibit backscatter (see Figs. 13 and 14). These nonlinear states are appealing since they combine topologically protected one-way motion with the robustness and balance of solitons.

V. CONCLUSIONS

Tight-binding approximations that describe deep longitudinally driven Lieb and Kagome waveguide lattices were constructed. These lattices were decomposed into three sublattices such that each sublattice moves with its own driving pattern e.g. phase offset, different radii,

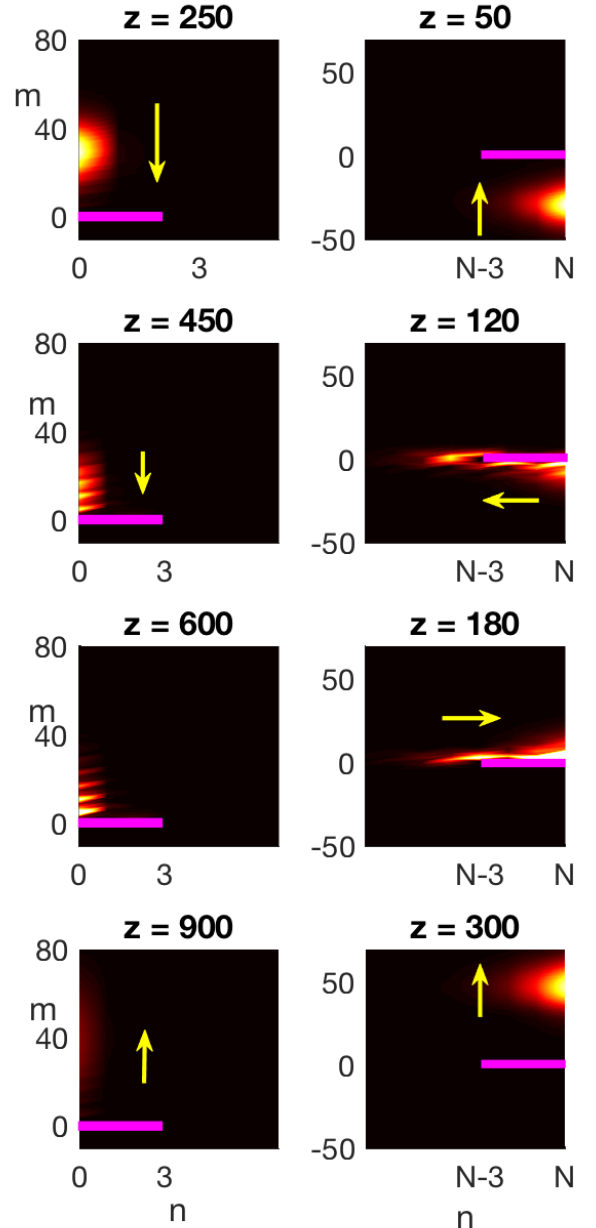


FIG. 14. Linear edge mode dynamics encountering a defect barrier in the Kagome lattice for in-phase rotation corresponding to the Floquet bands in Fig. 9(b). (Left column) Intensity evolution $|b_{mn}(z)|^2$ along pointy edge with same rotation and $(k_y, \alpha) = (1.2, .343)$. (Right column) Intensity evolution $|c_{mn}(z)|^2$ along straight edge and $(k_y, \alpha) = (1.2, -.178)$.

different frequency, etc. We considered periodically oscillating waveguides and computed their corresponding Floquet bands. These dispersion bands were found to support localized topologically protected edge modes that were either stationary (flat band) or traveling. A topological invariant, the Chern number was calculated; this demonstrates that there is nontrivial associated topology present in the dispersion bands.

Topologically protected modes located in the band gap with sign-definite group velocity throughout the gap were found to propagate unidirectionally around lattice de-

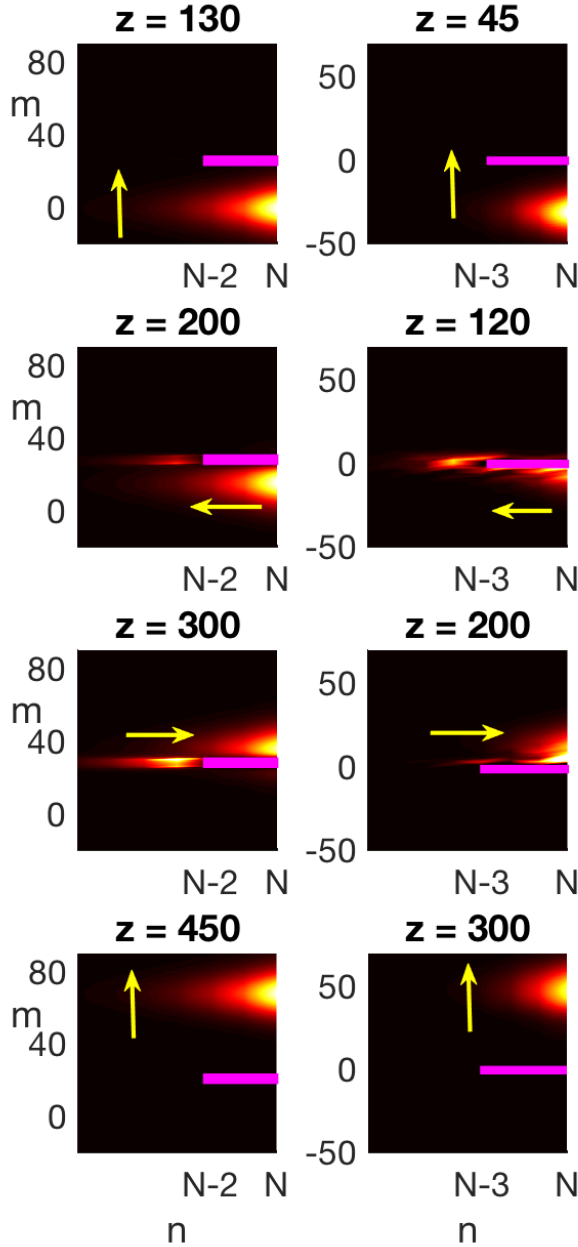


FIG. 15. Nonlinear ($\gamma_{nl} = \epsilon = 1/\Omega$) edge mode dynamics encountering a defect barrier. (Left column) Intensity, $|c_{mn}(z)|^2$, in Lieb lattice with same parameters as those given in right column of Fig. 12 with dispersion $\alpha''(1.65) = -.0364$ corresponding to Fig. 4(b). (Right column) Intensity, $|c_{mn}(z)|^2$, in Kagome lattice with same parameters as those given in right column of Fig. 14 with dispersion $\alpha''(1.2) = .141$ corresponding to Fig. 9(b).

fect barriers, and did not significantly backscatter. If, on the other hand, the corresponding Floquet band has sign-indefinite group velocity, then the edge mode could backscatter at the barrier. Additionally, when the corresponding Floquet exponent is not well-separated from the bulk band, then strong dispersion could occur. These observations highlight further insights regarding topologically protected modes.

Two additional conclusions can be drawn from this work: (i) Numerous physically significant lattices can be used to find topologically protected edge modes e.g. honeycomb, staggered square, Lieb, Kagome. The tight-binding approach we have developed can be generalized to incorporate more detailed features e.g. next-nearest neighbor interaction, detuning in the refractive index, etc. (ii) Many different types of longitudinal driving can generate topologically protected edge modes. Moreover, different rotation patterns can be selected to suit applications e.g. along the bearded edge of a Lieb lattice π -offset rotation creates faster propagating modes than in-phase rotation.

Finally, weakly nonlinear modes were found to inherit the topological protection of the linear Floquet modes. These modes present an exciting opportunity to merge the one-way properties of the linear problem with intense nonlinear states i.e. solitons.

VI. ACKNOWLEDGEMENTS

This work was partially supported by AFOSR under grant No. FA9550-16-1-0041.

[1] F. Haldane and S. Raghu, Phys. Rev. Lett. **100**, 013904 (2008).
 [2] Z. Wang, Y. Chong, J. Joannopoulos, and Soljačić, Nature **461**, 772 (2009).
 [3] M. C. Rechtsman, J. M. Zeuner, Y. Plotnik, Y. Lumer, S. Nolte, F. Dreisow, M. Segev, and A. Szameit, Nature **496**, 196 (2013).

[4] D. Leykam, M. C. Rechtsman, and Y. D. Chong, Phys. Rev. Lett. **117**, 013902 (2016).
 [5] D. Leykam and Y. D. Chong, Phys. Rev. Lett. **117**, 143901 (2016).
 [6] J. Noh, S. Huang, D. Leykam, Y. D. Chong, K. P. Chen, and M. C. Rechtsman, Nature Physics **13**, 611 (2017).

- [7] M. J. Ablowitz and J. T. Cole, Phys. Rev. A **96**, 043868 (2017).
- [8] Y. Lumer, M. C. Rechtsman, Y. Plotnik, and M. Segev, Phys Rev A **94**, 021801(R) (2016).
- [9] M. A. Bandres, M. C. Rechtsman, and M. Segev, Phys. Rev. X **6**, 011016 (2016).
- [10] X. Zhou, Y. Wang, D. Leykam, and Y. D. Chong, New J. Phys. **19**, 095002 (2017).
- [11] R. El-Ganainy and M. Levy, Opt. Lett. **40**, 5275 (2015).
- [12] W. Qiu, Z. Wang, and M. Soljačić, Opt. Express **19**, 22248 (2011).
- [13] B. Bahari, A. Ndao, F. Vallini, A. El Amili, Y. Fainman, and B. Kanté, Science (2017).
- [14] P. St-Jean, V. Goblot, E. Galopin, A. Lemaître, T. Ozawa, L. Le Gratiet, I. Sagnes, J. Bloch, and A. Amo, Nature Photonics **11**, 651 (2017).
- [15] M. Parto, S. Wittek, H. Hodaei, G. Harari, M. A. Bandres, J. Ren, M. C. Rechtsman, M. Segev, D. N. Christodoulides, and M. Khajavikhan, Phys. Rev. Lett. **120**, 113901 (2018).
- [16] M. A. Bandres, S. Wittek, G. Harari, M. Parto, J. Ren, M. Segev, D. N. Christodoulides, and M. Khajavikhan, Science (2018).
- [17] G. Harari, M. A. Bandres, Y. Lumer, M. C. Rechtsman, Y. D. Chong, M. Khajavikhan, D. N. Christodoulides, and M. Segev, Science (2018).
- [18] M. J. Ablowitz, C. Curtis, and Y.-P. Ma, Phys. Rev. A **90**, 023813 (2014).
- [19] N. Goldman, D. F. Urban, and D. Bercioux, Phys Rev A **83**, 063601 (2011).
- [20] G.-B. Jo, J. Guzman, C. K. Thomas, P. Hosur, A. Vishwanath, and D. M. Stamper-Kurn, Phys. Rev. Lett. **108**, 045305 (2012).
- [21] J. S. Helton, K. Matan, M. P. Shores, E. A. Nytko, B. M. Bartlett, Y. Qiu, D. G. Nocera, and Y. S. Lee, Phys. Rev. Lett. **104**, 147201 (2010).
- [22] D. Guzmán-Silva, C. Mejía-Cortés, M. A. Bandres, M. Rechtsman, S. Weimann, S. Nolte, M. Segev, A. Szameit, and R. A. Vicencio, New J. Phys. **16**, 063061 (2014).
- [23] R. A. Vicencio, C. Cantillano, L. Morales-Inostroza, B. Real, C. Mejía-Cortés, S. Weimann, A. Szameit, and M. I. Molina, Phys. Rev. Lett. **114**, 245503 (2015).
- [24] S. Mukherjee, A. Spracklen, D. Choudhury, N. Goldman, P. Öhberg, E. Andersson, and R. R. Thomson, Phys. Rev. Lett. **114**, 245504 (2015).
- [25] Y. Zong, S. Xia, L. Tang, D. Song, Y. Hu, Y. Pei, J. Su, Y. Li, and Z. Chen, Opt. Express **24**, 8877 (2016).
- [26] M. A. Bandres, M. C. Rechtsman, A. Szameit, and M. Segev, CLEO:2014 OSA Technical Digest, FF2D.3 (2014).
- [27] R. A. Vicencio and C. Mejía-Cortés, J. Opt. **16**, 015706 (2014).
- [28] A. Szameit and S. Nolte, J. Phys. B: At. Mol. Opt. Phys. **43**, 163001 (2010).
- [29] N. Marzari, A. A. Mostofi, J. R. Yates, I. Souza, and D. Vanderbilt, Rev. Mod. Phys. **84**, 1419 (2012).
- [30] Y. Hatsugai, Phys. Rev. Lett. **71**, 3697 (1993).
- [31] L. Lu, J. Joannopoulos, and M. Soljačić, Nature Photonics **8**, 821 (2014).
- [32] M. S. Rudner, N. H. Lindner, E. Berg, and M. Levin, Phys. Rev. X **3**, 031005 (2013).
- [33] T. Fukui, Y. Hatsugai, and H. Suzuki, J. Phys. Soc. Jpn. **74**, 1674 (2005).

Appendix A: Tight-binding Model Coefficients

The coefficients in the tight-binding models given in Sec. II are presented here. The Lieb (16)-(18) and Kagome (23)-(25) systems are both defined in terms of the distance-dependent coefficient $\mathbb{L}(\mathbf{v})$. The only difference in the two tight-binding models is the individual lattice configurations i.e. the different lattice vectors between nearest neighbor lattice sites, and the driving pattern being used. We point out that we neglect a small imaginary coefficient \mathbb{R}_j that was used in [7]. The reason is that typically V_0 is large and so $|\mathbb{L}(\mathbf{v})| \gg 1$ is the asymptotically dominant term. As a result, the numerically computed spectrum of the Lieb and Kagome systems in Sec. II is found to be real.

The linear coefficient in the tight-binding approximations is

$$\begin{aligned} \mathbb{L}(\mathbf{v} - \Delta \mathbf{h}_{ij}(z)) &= \left[V_0^3 \sqrt{\frac{\sigma_x \sigma_y}{(1 + \sigma_x V_0)(1 + \sigma_y V_0)}} \right. & (A1) \\ &\times \left(2e^{-\frac{V_0}{4} \left[\frac{[\mathbf{v} - \Delta \mathbf{h}_{ij}(z)]_x^2}{\sigma_x(1 + V_0 \sigma_x)} + \frac{[\mathbf{v} - \Delta \mathbf{h}_{ij}(z)]_y^2}{\sigma_y(1 + V_0 \sigma_y)} \right]} - 1 \right) \\ &+ \frac{V_0^2}{4} \left(\frac{[\mathbf{v} - \Delta \mathbf{h}_{ij}(z)]_x^2}{\sigma_x^2} + \frac{[\mathbf{v} - \Delta \mathbf{h}_{ij}(z)]_y^2}{\sigma_y^2} \right) \\ &\times e^{-\frac{V_0}{4} \left(\frac{[\mathbf{v} - \Delta \mathbf{h}_{ij}(z)]_x^2}{\sigma_x} + \frac{[\mathbf{v} - \Delta \mathbf{h}_{ij}(z)]_y^2}{\sigma_y} \right)} \Big] e^{i\mathbf{v} \cdot \mathbf{A}(z)}, \end{aligned}$$

where the x and y subscripts denote the first and second components, respectively. The relative driving motion is captured by the functions $\Delta \mathbf{h}_{ij}(z) \equiv \mathbf{h}_i(z) - \mathbf{h}_j(z)$ for $i, j = a, b, c$. The defining lattice vectors for the Lieb and Kagome lattices are given in Eq. (14) and (15), respectively. The nonlinearity coefficient for the tight-binding models is given by

$$\gamma_{\text{nl}} = \frac{\gamma V_0}{2\pi \sqrt{\sigma_x \sigma_y}} \geq 0.$$

Appendix B: Computation of Chern Numbers

Bulk bands with associated nontrivial Chern numbers are known to support gapless edge modes [31]. The Chern number for a bulk band is equal to the number of gapless modes above the band minus the number of gapless modes below it. The orientation of the chirality must also be taken into account: modes moving in the counter-clockwise (clockwise) direction have a positive (negative) chirality. This is reflected in the Chern numbers, in particular in the quasi 1d motion case (36), where the edge modes travel clockwise around the boundary and the corresponding Chern numbers have opposite sign. Moreover, the Chern invariants in the spectral problem [see Eq. (B2)] are the same as those in the edge problem. When a defect along the boundary is introduced the Chern invariants are unaffected and a topologically protected mode will persist. This is the Bulk-Edge correspondence. Hence our interests are served by computing the Chern invariants in order to establish whether

or not the modes we find are indeed topologically protected.

The Chern number of the bulk (spectral) bands is computed directly from the Lieb (16)-(18) and Kagome (23)-(25) discrete systems. For both systems we take plane wave solutions of the form

$$\begin{aligned} a_{mn} &= \delta(\mathbf{k}, z) e^{i\mathbf{k} \cdot (m\mathbf{w}_1 + n\mathbf{w}_2)}, \\ b_{mn} &= \beta(\mathbf{k}, z) e^{i\mathbf{k} \cdot (m\mathbf{w}_1 + n\mathbf{w}_2)}, \\ c_{mn} &= \gamma(\mathbf{k}, z) e^{i\mathbf{k} \cdot (m\mathbf{w}_1 + n\mathbf{w}_2)}, \end{aligned} \quad (\text{B1})$$

where $\mathbf{w}_1 = 2\mathbf{e}_2, \mathbf{w}_2 = 2\mathbf{e}_1$ for the Lieb lattice and $\mathbf{w}_1 = \mathbf{e}_2, \mathbf{w}_2 = \sqrt{3}\mathbf{e}_1$ for Kagome. Substituting (B1) into the tight-binding equations yields a 3×3 coupled system of equations

$$\frac{d\mathbf{c}}{dz} = i\mathcal{M}(\mathbf{k}, z)\mathbf{c}, \quad \mathbf{c} = (\delta, \beta, \gamma)^T, \quad (\text{B2})$$

such that

$$\mathcal{M}_{\text{Lieb}}(\mathbf{k}, z) = \begin{pmatrix} \Delta\mathbf{h}_{ab} \cdot \mathbf{A}_z & \mathbb{L}_1^{ab}(z) + \mathbb{L}_{-1}^{ab}(z)e^{-i\mathbf{k} \cdot 2\mathbf{e}_1} & 0 \\ \mathbb{L}_1^{ba}(z)e^{i\mathbf{k} \cdot 2\mathbf{e}_1} + \mathbb{L}_{-1}^{ba}(z) & 0 & \mathbb{L}_2^{bc}(z) + \mathbb{L}_{-2}^{bc}(z)e^{-i\mathbf{k} \cdot 2\mathbf{e}_2} \\ 0 & \mathbb{L}_2^{cb}(z)e^{i\mathbf{k} \cdot 2\mathbf{e}_2} + \mathbb{L}_{-2}^{cb}(z) & \Delta\mathbf{h}_{cb} \cdot \mathbf{A}_z \end{pmatrix},$$

for the Lieb lattice, where $\mathbb{L}_{\pm l}^{ij}(z) = \mathbb{L}(\pm\mathbf{e}_l - \Delta\mathbf{h}_{ij}(z))$,

and in the case of the Kagome lattice, the matrix is

$$\mathcal{M}_{\text{Kagome}}(\mathbf{k}, z) = \begin{pmatrix} \Delta\mathbf{h}_{ab} \cdot \mathbf{A}_z & \mathbb{L}_{-1}^{ab}(z) + \mathbb{L}_1^{ab}(z)e^{i\mathbf{k} \cdot (\mathbf{w}_1 + \mathbf{w}_2)} & \mathbb{L}_{-3}^{ac}(z) + \mathbb{L}_3^{ac}(z)e^{i\mathbf{k} \cdot (2\mathbf{w}_1)} \\ \mathbb{L}_{-1}^{ba}(z)e^{-i\mathbf{k} \cdot (\mathbf{w}_1 + \mathbf{w}_2)} + \mathbb{L}_1^{ba}(z) & 0 & \mathbb{L}_{-2}^{bc}(z)e^{-i\mathbf{k} \cdot (\mathbf{w}_2 - \mathbf{w}_1)} + \mathbb{L}_2^{bc}(z) \\ \mathbb{L}_{-3}^{ca}(z)e^{-i\mathbf{k} \cdot (2\mathbf{w}_1)} + \mathbb{L}_3^{ca}(z) & \mathbb{L}_{-2}^{cb}(z) + \mathbb{L}_2^{cb}(z)e^{i\mathbf{k} \cdot (\mathbf{w}_2 - \mathbf{w}_1)} & \Delta\mathbf{h}_{cb} \cdot \mathbf{A}_z \end{pmatrix},$$

where here $\mathbb{L}_{\pm l}^{ij}(z) = \mathbb{L}(\pm\mathbf{v}_l - \Delta\mathbf{h}_{ij}(z))$ for the vectors $\mathbf{v}_l, l = 1, 2, 3$ given in Eq. (15). The eigenmode solutions are computed via Floquet theory in a manner similar to that described above Eq. (30). The 2d Chern number for the p^{th} spectral band is defined by the following integral over the Brillouin zone (BZ)

$$C_p = \frac{1}{2\pi i} \iint_{\text{BZ}} (\nabla_{\mathbf{k}} \times \mathbf{A}_p) \cdot \hat{k} d\mathbf{k}, \quad (\text{B3})$$

in terms of the Berry connection $\mathbf{A}_p(\mathbf{k}, z) = \mathbf{c}_p^\dagger(z; \mathbf{k}) \partial_{k_x} \mathbf{c}_p(z; \mathbf{k}) \hat{\mathbf{i}} + \mathbf{c}_p^\dagger(z; \mathbf{k}) \partial_{k_y} \mathbf{c}_p(z; \mathbf{k}) \hat{\mathbf{j}}$, for the eigenmode $\mathbf{c}_p(z; \mathbf{k})$ corresponding to the p^{th} spectral band, evaluated at any z (see Appendix D), where $\nabla_{\mathbf{k}}$ is the gradient in \mathbf{k} , and \dagger denotes the complex conjugate transpose. Here we evaluate the Chern number at $z = 0$.

To numerically calculate the Chern numbers (B3) the algorithm proposed in [33] is used and summarized below. Consider a square lattice with period ℓ . Any non-square lattice can be mapped to a square lattice by a linear transformation. In the algorithm, a square Brillouin zone $[0, 2\pi/\ell) \times [0, 2\pi/\ell)$ is discretized by

$$\mathbf{k}_{rs} = \left(\frac{2\pi r}{\ell N}, \frac{2\pi s}{\ell N} \right), \quad r, s = 0, 1, \dots, N-1. \quad (\text{B4})$$

The so-called unitary link variable is given by

$$U_{\mu, \nu}(\mathbf{k}_{rs}) = \frac{\mathbf{c}_p^*(\mathbf{k}_{rs}) \mathbf{c}_p(\mathbf{k}_{r+\mu, s+\nu})}{|\mathbf{c}_p^*(\mathbf{k}_{rs}) \mathbf{c}_p(\mathbf{k}_{r+\mu, s+\nu})|}, \quad (\text{B5})$$

where $\mu, \nu = 0, 1$. Normalizing the link variables this way isolates the phase. The Berry curvature at the point \mathbf{k}_{rs} is approximated by

$$F(\mathbf{k}_{rs}) = \ln \left[\frac{U_{1,0}(\mathbf{k}_{rs}) U_{0,1}(\mathbf{k}_{r+1,s})}{U_{1,0}(\mathbf{k}_{r,s+1}) U_{0,1}(\mathbf{k}_{rs})} \right]. \quad (\text{B6})$$

Finally, the Chern number integral in (B3) is approximated by the sum

$$\tilde{C}_p = \frac{1}{2\pi i} \sum_{r,s} F(\mathbf{k}_{rs}). \quad (\text{B7})$$

In the limit $N \rightarrow \infty$ it can be shown that $\tilde{C}_p \rightarrow C_p$.

Appendix C: Floquet Bands for Honeycomb and Staggered Square Lattices

In our studies we have observed that quite often similar sublattice driving patterns yield similar Floquet band structure, regardless of the underlying lattice. To emphasize this point we will show typical dispersion bands corresponding to the honeycomb and staggered square lattices [7] for rotation parameters similar to those considered above. These lattices possess two lattice sites per unit cell, unlike the three lattice sites per unit cell for Lieb and Kagome. In terms of the discrete systems given in Sec. II, these simpler systems are written in a similar

form but with a equations instead: see [7]. Moreover, we compute the Chern numbers to establish that there are topologically protected edge modes. One difference between the bands computed in [7] and those shown here is that we neglect the \mathbb{R}_j term in the linear coefficients i.e. $\mathbb{L}_+(\mathbf{v}) \rightarrow \mathbb{L}(\mathbf{v})$. The justifications are discussed in Appendix A.

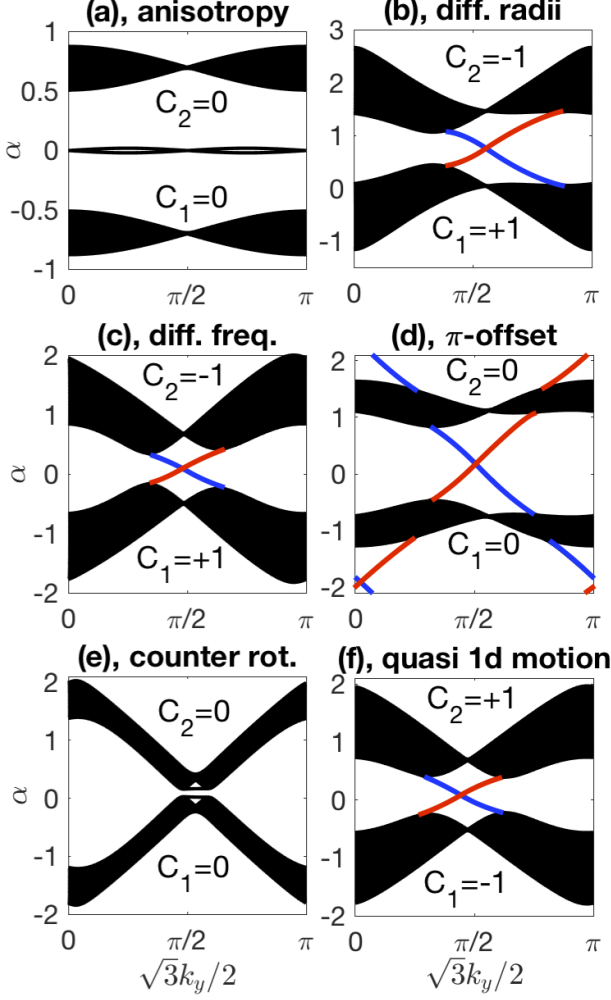


FIG. 16. (Color online) Honeycomb Floquet bands for various rotation patterns with zig-zag boundary conditions. Red curves indicate gapless edge modes on right edge, blue curves denote left gapless edge modes. The parameters used are the same as in Fig. 10 with $a_{mn}(z) = 0$, except (e) where $\eta = 2.2/15$.

The Floquet bands for a typical honeycomb lattice are shown in Fig. 16. The parameters are identical to those used in Fig. 10, except where noted. In the case of anisotropy [Fig. 16(a)], the non-topological edge bands do not span the gap and the Chern numbers are trivial. Topologically protected traveling modes are observed in the case of different radii [Fig. 16(b)], different frequency [Fig. 16(c)], π -offset [Fig. 16(d)] and quasi 1d motion [Fig. 16(f)]. Since there are the same number of chiral modes above and below the π -offset bulk bands, the corresponding Chern numbers are zero. The edge modes

found in the case of counter rotation [see Fig. 16(e)] do not span the gap or travel i.e. $\alpha'(k_y) = 0$.

Similar to the Lieb and Kagome lattices, the π -offset rotation has an additional family of solutions located at the Floquet edge. Unlike the other lattices, the honeycomb lattice possesses non-topological modes in the case of anisotropy. The modes for quasi 1d motion are found to travel in propagate in the opposite direction relative to all other rotation patterns, just like the Lieb, Kagome and square lattices (see below). Since the edge modes travel with opposite chirality, the sign of the corresponding Chern numbers is also inverted: the lower (upper) bulk band has a Chern number of $-1(+1)$.

The next set of band diagrams are for the staggered square lattice (see Fig. 17). In this case the underlying lattice is actually simple when the two sublattices rotate in phase with each other. As a result, for in-phase rotation with anisotropic waveguides we obtain the bands in Fig. 17(a) that only have one bulk band and do not support any edge modes.

By driving two sublattices in different patterns topological edge modes can be generated. Traveling unidirectional/topological modes are generated by different radii [Fig. 17(b)], different frequency [Fig. 17(c)], π -offset [Fig. 17(d)], counter rotation [Fig. 17(e)], and quasi 1d motion [Fig. 17(f)]. The different frequency [Fig. 17(c)] and π -offset [Fig. 17(d)] bands possess a parameter regime with a “mini-gap” that is numerically challenging to resolve. As a result, we do not include their Chern numbers, but do note that the modes in the upper and lower gaps exhibit robust unidirectional motion characteristic of topologically protected states.

Like each other case considered above, the π -offset rotation pattern has a radius threshold necessary to generate the modes shown in Fig. 17(d). For the different radii bands shown in Fig. 17(b) additional nontopological modes are found near $\alpha = 1$, and the Chern numbers reflect this. The central gap modes in counter rotation, and quasi 1d motion do span the gap and are topologically protected, dissimilar to the honeycomb lattice above. Similar to the Lieb, Kagome, and honeycomb lattices, modes generated from the quasi 1d motion propagate in an opposite orientation i.e. chirality, relative to most other cases.

Appendix D: Chern Number Invariance

In Appendix B the Chern number (B3) and Bulk-Edge correspondence were computed and discussed. The eigenfunctions in (B2) depend on z (in general) and it is not clear that the Chern number is an invariant quantity i.e. $C(z) = \text{constant}$. The purpose of this appendix is to prove that the Chern number is a z -independent quantity by showing $\frac{dC}{dz} = 0$. We show this for the Lieb lattice (the Kagome lattice follows in a similar manner).

Recall, for system (B2), the 2d Chern number is

$$C = \frac{1}{2\pi i} \iint_{BZ} \left(\frac{\partial \mathbf{c}^\dagger}{\partial k_x} \frac{\partial \mathbf{c}}{\partial k_y} - \frac{\partial \mathbf{c}^\dagger}{\partial k_y} \frac{\partial \mathbf{c}}{\partial k_x} \right) dk_x dk_y, \quad (\text{D1})$$

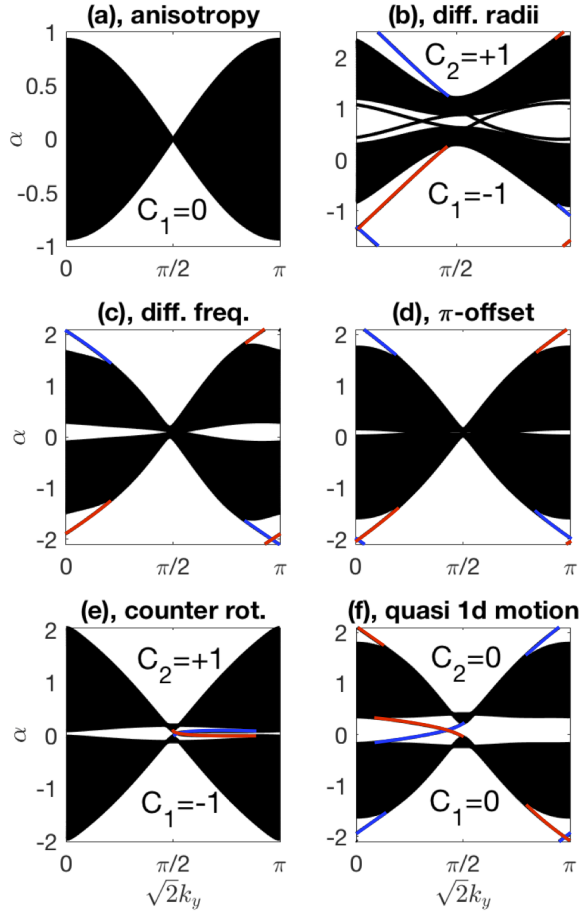


FIG. 17. (Color online) Staggered square Floquet bands for various rotation patterns. Red curves indicate gapless edge modes on right edge, blue curves denote left gapless edge modes. The parameters used are the same as in Fig. 10 with $a_{mn}(z) = 0$, except (d) and (e) where $\eta = 1.5/15$.

where \dagger denotes the complex conjugate transpose. One key observation is the symmetry in the linear coefficients (A1):

$$\mathbb{L}_{-\ell}^{ij} = \mathbb{L}(-\mathbf{v}_\ell - \Delta \mathbf{h}_{ij}) = \mathbb{L}^*(\mathbf{v}_\ell - \Delta \mathbf{h}_{ji}) = \left(\mathbb{L}_\ell^{ji} \right)^*, \quad (\text{D2})$$

where $*$ denotes complex conjugation. The Brillouin zone for the Lieb lattice in Fig. 1 is the square $[0, \pi] \times [0, \pi]$. The Lieb coefficient matrix below (B2) is periodic $\mathcal{M}(k_x + \pi, k_y, z) = \mathcal{M}(k_x, k_y, z) = \mathcal{M}(k_x, k_y + \pi, z)$ and, by symmetry (D2), Hermitian: $\mathcal{M}^\dagger = \mathcal{M}$.

Differentiating (B3) with respect to z yields

$$\frac{dC}{dz} = \frac{1}{2\pi} \iint_0^\pi \left(\frac{\partial \mathbf{c}^\dagger}{\partial k_x} \frac{\partial \mathcal{M}}{\partial k_y} \mathbf{c} + \mathbf{c}^\dagger \frac{\partial \mathcal{M}}{\partial k_y} \frac{\partial \mathbf{c}}{\partial k_x} - \mathbf{c}^\dagger \frac{\partial \mathcal{M}}{\partial k_x} \frac{\partial \mathbf{c}}{\partial k_y} - \frac{\partial \mathbf{c}^\dagger}{\partial k_y} \frac{\partial \mathcal{M}}{\partial k_x} \mathbf{c} \right) dk_x dk_y. \quad (\text{D3})$$

We assume that if the eigenfunction \mathbf{c} is periodic in \mathbf{k} at $z = 0$: $\mathbf{c}(k_x + \pi, k_y, z = 0) = \mathbf{c}(k_x, k_y, z = 0) = \mathbf{c}(k_x, k_y + \pi, z = 0)$, then \mathbf{c} remains periodic in \mathbf{k} for all z . Applying integration-by-parts on (D3), along with

$\frac{\partial^2 \mathcal{M}}{\partial k_x \partial k_y} = 0$, gives the desired result. Hence the Chern numbers in Eq. (B3) are independent of z .